ciRS-7 and miR-7 regulate ischemia induced neuronal death via glutamatergic signaling

Flavia Scoyni[1]*, Valeriia Sitnikova[1]†, Luca Giudice[1]†, Paula Korhonen[1], Davide M Trevisan[2], Ana Hernandez de Sande[3], Mireia Gomez-Budia[1], Raisa Giniatullina[1], Irene F Ugidos[1], Hiramani Dhungana[4], Cristiana Pistono[1], Nea Korvenlaita[1], Nelli-Noora Välimäki[1], Salla M Kangas[5], Anniina E Hiltunen[6], Emma Gribchenko[1], Minna U Kaikkonen-Määttä[1], Jari Koistinaho[1,4], Seppo Ylä-Herttuala[1], Reetta Hinttala[5,6], Morten T Venø[7,8], Junyi Su[8], Markus Stoffel[9], Anne Schaefer[10,11], Nikolaus Rajewsky[12], Jørgen Kjems[8], Mary P LaPierre[9], Monika Piwecka[13], Jukka Jolkkonen[1], Rashid Giniatullin[1], Thomas B Hansen[8, ‡], Malm Tarja[1]*

Affiliations:

[1]A.I.Virtanen Institute for Molecular Sciences, University of Eastern Finland, Kuopio, 70221, Finland

[2]Department of Biosciences and Nutrition, Karolinska Institute, Stockholm, 17177, Sweden

[3]School of Medicine, University of Eastern Finland, Kuopio, 70221, Finland

[4]Neuroscience Center, University of Helsinki, Helsinki, 00290, Finland

[5]Biocenter Oulu, University of Oulu, Oulu, 90014, Finland

[6]Medical Research Center Oulu and Research Unit of Clinical Medicine, University of Oulu and Oulu University Hospital, Oulu, 90014, Finland

[7]Omiics ApS, Aarhus, 8200, Denmark

[8]Interdisciplinary Nanoscience Center, Department of Molecular Biology and Genetics, Aarhus University, Aarhus, 8000, Denmark

[9]Institute of Molecular Health Sciences, ETH Zurich, Zürich, 8093, Switzerland

[10]Departments of Neuroscience and Psychiatry, Icahn School of Medicine at Mount Sinai, New York, 10029-6504, USA

[11]Max Planck Institute, Biology of Ageing, Cologne, 50931, Germany

[12]Systems Biology of Gene Regulatory Elements, Max-Delbrück-Center for Molecular Medicine in the Helmholtz Association (MDC), Berlin Institute for Medical Systems Biology (BIMSB), Berlin, 10115, Germany

[13]Institute of Bioorganic Chemistry, Polish Academy of Sciences, Poznan, 61-704, Poland

*Correspondence: flavia.scoyni@uef.fi and tarja.malm@uef.fi;

† These authors contributed equally; ‡ Present address: Targovax ASA, Lysaker, 1366, Norway

ABSTRACT

Brain functionality relies on finely tuned regulation of gene expression by networks of non-coding RNAs (ncRNAs) such as the one composed by the circular RNA ciRS-7 (also known as CDR1as), the microRNA miR-7 and the long non-coding RNA Cyrano. Here we describe ischemia induced alterations in the ncRNA network both *in vitro* and *in vivo* and in transgenic mice lacking ciRS-7 or miR-7. Our data show that cortical neurons downregulate ciRS-7 and Cyrano and upregulate miR-7 expression upon ischemic insults. Mice lacking ciRS-7 show reduced lesion size and motor impairment, whilst the absence of miR-7 alone leads to an increase in the ischemia induced neuronal death. Moreover, miR-7 levels in pyramidal excitatory neurons regulate dendrite morphology and glutamatergic signaling suggesting a potential molecular link to the *in vivo* phenotype. Our data reveal that ciRS-7 and miR-7 contribute to the outcome of ischemic stroke and shed new light into the pathophysiological roles of intracellular networks of non-coding RNAs in the brain.

INTRODUCTION

The intricate functionality of the brain relies on precisely regulated gene expression, also mediated by non-coding RNAs (ncRNAs), molecules abundant in the brain linked to the increased cognitive complexity in human[1]. MicroRNAs (miRNAs), short (~22 nucleotides) ncRNAs, post-transcriptionally regulate messenger RNA (mRNA) expression by binding short complementary sequences (seed)[2] and triggering mRNA decay or inhibition of translation[3]. Long non-coding RNAs (lncRNAs), RNA molecules longer than 200 nucleotides, regulate gene expression by interacting with other ncRNAs, including miRNAs, or proteins[4]. Circular RNAs (circRNAs), a novel class of ncRNAs, modulate gene expression also by interacting with miRNAs, hence affecting miRNAs activity on mRNA targets[5]. CircRNAs result from backsplicing of linear transcripts, an uncanonical splicing event in which a 5' splice site is spliced with the 3' splice site of the upstream exon[6], forming a circular molecule.

These ncRNAs independently control cellular function by regulating the expression of protein-coding genes, but also interact with each other. In the brain-specific ncRNA network involving miR-7, miR-671, the lncRNA Cyrano and the circRNA ciRS-7 (also known as CDR1as)[5,7–9], ciRS-7 is suggested to stabilize and promote miR-7 targeting[8,9], while Cyrano triggers miR-7 degradation via target RNA–directed miRNA degradation (TDMD)[8] with a nearly perfectly complementary binding site. Analysis through gain and loss of function experiments and knock-out animals revealed that Cyrano and ciRS-7 bind miR-7, regulating its expression[5,8,9] and that Cyrano TDMD effect on miR-7 affects ciRS-7 abundance and localization, indirectly affecting the gene expression of miR-7 targets[5,8–10]. Nonetheless, the physiological purpose of this network in the brain remains unknown, including lack of information on its role in pathophysiological conditions.

Ischemic stroke, induced by occlusion of one of the major cerebral arteries, leads nutrients and oxygen deprivation in the brain parenchyma inducing cell death. Lack of energy and disruption in the ion balance cause an uncontrolled release of glutamate in excitatory neurons, leading to excitotoxicity[11], oxidative stress, necrosis, and apoptosis[12]. Various miRNAs and lncRNAs have been implicated in regulating oxidative stress response and glutamate excitotoxicity, impacting stroke outcomes[13]. Sustained stress prompts miRNAs to facilitate adaptive switches in gene expression program[14]. The efficiency of the miRNA-mediated response depends on miRNAs availability to interact (expression, localization, activity) and the amount of mRNA targets possessing a Mirna Recognition Element (MRE), creating a miRNA-specific threshold[15]. Sudden changes in MRE-containing sequences can disrupt miRNA targeting and derepress specific targets. This crosstalk led to theorize that in physiological conditions a large number of MRE sequences compete for the binding of the miRNA[16]. Organisms exploit this phenomenon during stress by regulating miRNA activity through transcripts with varying binding strength or MRE abundance following a process called target mimicry[17].

Recent studies emphasize a strong connection between circRNAs and reactive oxygen species production[18]. Despite individual ncRNAs being studied in the context of ischemic stroke[13], a comprehensive analysis of the regulatory role of ncRNAs network in stroke is still lacking. In this study, we identified ciRS-7, brain enriched circRNA, ciRS-7, among seven circRNAs deregulated in ischemia-related conditions *in vitro* and *in vivo*. Expanding our analysis to other ncRNAs species, we identified changes in miR-7 and Cyrano, part of the same regulatory circuitry as ciRS-7. Using ciRS-7 and miR-7 knock-out mouse models, we revealed the potential role of ciRS-7 in preventing miR-7-mediated regulation of the target mRNAs, unveiling the contribution of ciRS-7 molecular network in preventing stroke-induced cell death.

49 **RESULTS**

50 ***Oxygen and glucose deprivation induces changes in the expression of circular RNAs***

51 Given the association of circRNAs with oxidative stress response[18] we evaluated their potential
52 deregulation in conditions mimicking ischemic stroke *in vitro*. We cultured murine cortical neurons
53 isolated from embryonic day fifteen (E15) cortices, subjected them to oxygen and glucose deprivation
54 (OGD) for 12 hours (Supplementary Figure S1A) and performed total RNA sequencing.

55 A deconvolution analysis on single-cell RNA-seq dataset of embryonic mouse brain (E14.5[19])
56 confirmed that our culture is representative of the murine cortex, identifying interneurons (Int) and
57 pyramidal neurons (Layer V-VI) as the predominant cell populations (Figure 1A). Functional
58 validation using calcium imaging recording upon GABA and glutamate stimulation revealed that our
59 culture primarily consists of glutamatergic excitatory neurons, as 98% of cells in our culture
60 responded to glutamate and 36% to GABA (Figure 1B).

61

62 Ingenuity Pathway Analysis (IPA) of the differentially expressed genes between normoxic and OGD
63 neurons confirmed the activation of Hypoxia-inducible factor 1-alpha (HIF-1alpha) (Figure 1C) and
64 downstream upregulation of glycolysis, a characteristic hallmark of OGD[20] (Supplementary Table
65 S1, Supplementary Figure S1B). Moreover, colorimetric cell viability assay indicated 30% decrease
66 in neuronal viability post-exposure (Supplementary Figure S1C), confirming vulnerability to
67 ischemia-induced cell death.

68 CircRNAs, generated by back-splicing, are identified through back-splice junction reads (BSJ)
69 spanning regions that are not present in regularly spliced transcripts (forward splice junction reads,
70 FSJ) (Figure 1D). By using *CIRIquant* algorithm[21], which comprises several circRNAs identification
71 tools, we identified 27 circRNAs with high confidence, of which 7 were significantly differentially
72 expressed (DE) between normoxic (control) and OGD conditions (Figure 1E, Supplementary Table

73 S2). Notably, ciRS-7 was the most expressed circRNA yielding the highest number of back-splice
74 junctions (Figure 1F, left) and the highest circular to linear ratio (Junction ratio) (Figure 1F, right).
75 The obtained junction ratio score of above 0.88, indicate that the transcript generated by the ciRS-7
76 locus are over 88% in circular form, while other circRNAs exhibited only 40% of circular expression.
77 Specifically, ciRS-7 was one of the three downregulated circRNAs upon OGD with a log_2FC of -
78 0.552.

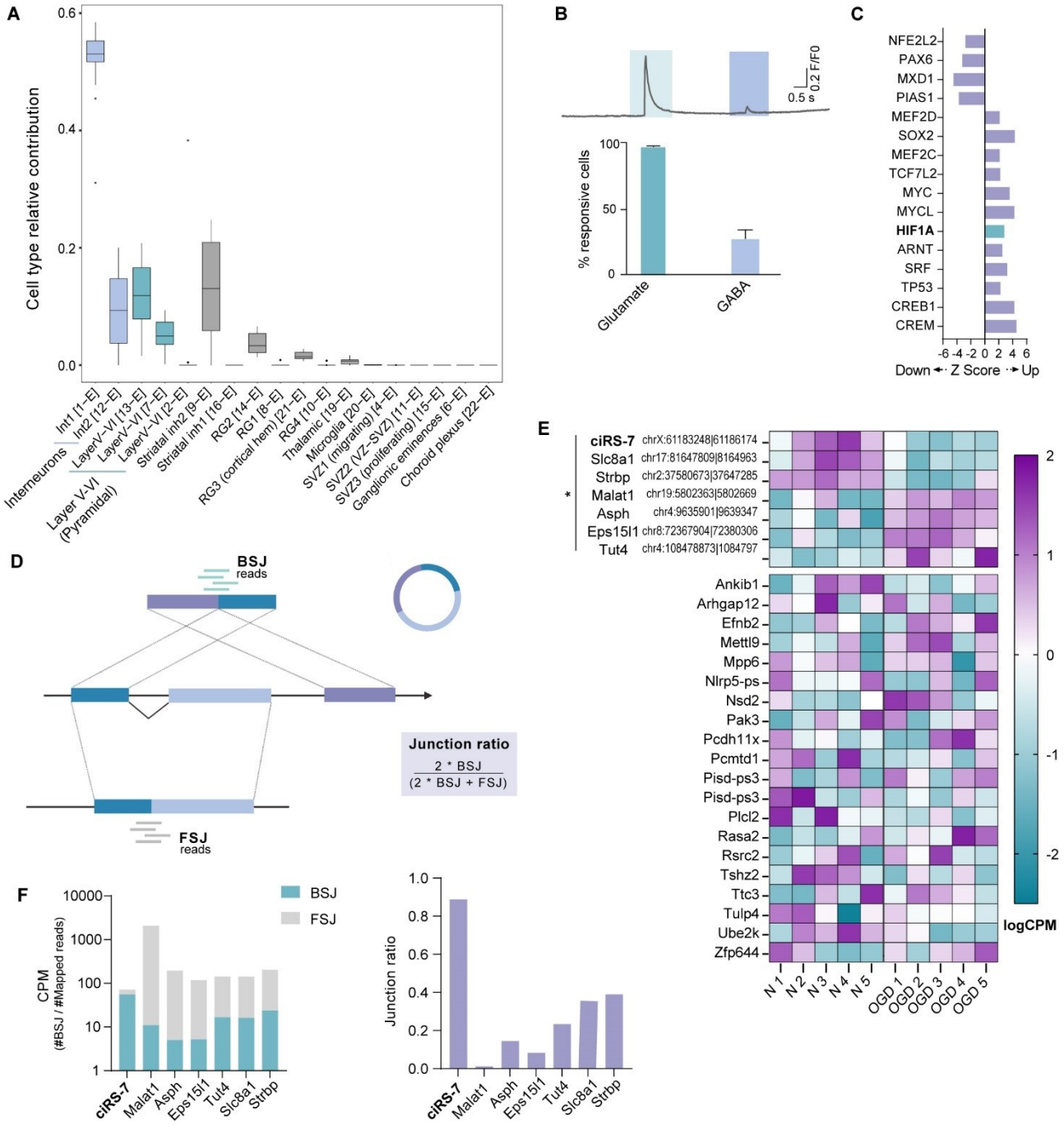

79

80 **Figure 1. ciRS-7 is the most abundant circRNA in mouse cortical neuron cultures and**

81 **downregulated by in vitro OGD.**

82 **(A)** Box plot of bulk RNA-seq deconvolution scores, indicating neuronal type contributions to overall

83 gene expression profile. X-axis labels derive from initial categorization by the authors of the dataset

84 (GSE123335), sorted by median of universal semantic groups (e.g., Int1, Int2 in Interneurons). **(B)**

85 Calcium imaging analysis of cellular response to glutamate and GABA with representative trace (n =
86 11; signal > 5% of baseline; mean ± SD). **(C)** Bar plot of Ingenuity Pathway Analysis (IPA) of bulk
87 RNA-seq data from OGD-treated cortical neurons. Z-score denotes prediction of transcription factor
88 activation (positive) or inhibition (negative); significant HIF1α activation is highlighted in green (|z|
89 > 2 is considered significant). **(D)** Schematic of CIRIquant algorithm: Gene with three exons (dark
90 blue, light blue, purple) produces a circular molecule via back-splicing or a linear transcript. Green
91 bars denotes specific circular reads on back-splice junction (BSJ), the reads from forward splicing
92 junctions (FSJ) in the same region are in gray. The Junction ratio score formula calculates a
93 circularization score, indicating the percentage of the gene in circular form. **(E)** Heat map of logCPM
94 for detected circRNAs in normoxic (N) and oxygen/glucose-deprived (OGD) murine cortical
95 neurons. Green indicates low expression, while purple indicates high expression. Significantly
96 differentially expressed circRNAs are grouped with a bar (* = adj. p-value < 0.05, n = 5). **(F)** (*left*)
97 Bar plot of CPM of the BSJ and FSJ of differentially expressed circularRNAs between normoxic and
98 OGD conditions, BSJ represents circular specific reads. (*right*) Bar plot of the Junction ratio score
99 bar plot from CIRIquant algorithm, showing the ratio of BSJ to FSJ reads mapped to the BSJ site and
100 indicating the percentage of circularization relative to the linear transcript.

101 ***ciRS-7 network is altered in conditions mimicking ischemic stroke in vitro***

102 ciRS-7 is part of a feedback loop with miR-671 and miR-7 microRNA[5,7] and indirectly, through miR-
103 7, with the long non-coding RNA Cyrano[8] (Figure 2A). To investigate the relative expression of these
104 players in *in vitro* OGD conditions, we performed small RNA sequencing of cortical neurons exposed
105 to OGD for 12h. Together with the previously presented dataset, we were able to capture circRNAs,
106 mRNAs, long non-coding RNAs and small RNA transcripts (Supplementary Table S2).

107

108 Small RNA-sequencing identified 333 upregulated and 88 downregulated miRNAs following OGD
109 (Figure 2B). Notably, the levels of miR-671-5p remained unaltered (Figure 2B) which was confirmed

110 independently by RT-qPCR (Supplementary Figure S2A), in contrast to previous reports of divergent
111 miR-671-5p and ciRS-7 expression in different contexts[7–9]. Instead, we detected a significant
112 upregulation in miR-7a-5p, but not of the variant miR-7b-5p (Figure 2B, Supplementary Table S2).
113 Similarly to human, in mouse miR-7 is redundantly encoded by three different loci (*miR-7a-1*, *miR-*
114 *7a-2*, *miR-7b*), each produced from different primary transcript (pri-miRNA) and precursor (pre-
115 miRNA). Further processing, in all cases from -5p arm, give rise to two mature miR-7 sequences
116 (miR-7a and miR-7b), differing only by a single nucleotide in the non-seed position number 10
117 (Figure 2C). To study the expression of the three miR-7 loci in our system, we utilized Global run-
118 on sequencing (GRO-seq), which enable the capture of nuclear nascent RNA primary molecules, and
119 compared the expression in our murine culture[22] with different mouse tissues and cell lines[22–32]
120 (Supplementary Table S3). In physiological conditions, only cortical neurons and the pituitary gland
121 actively transcribe all three independently regulated *miR-7* loci (Figure 2D, Supplementary figure
122 S3). The active transcription from three different loci in neuronal cells suggests a higher order of
123 regulation of this miRNA which influences the mature forms. Under OGD conditions, only the pri-
124 miRNAs contributing to the expression of miR-7a (miR-7a-1 and miR-7a-2) were significantly
125 upregulated (Figure 2E), indicating that the observed upregulation occurs already at the level of
126 transcription. None of miR-7 passenger strands generated from the three precursors (miR-7a-1-3p,
127 miR-7a-2-3p, and miR-7b-3p) were altered in our sequencing data (Supplementary Table S2).
128 Moreover, we detected no changes in the host gene in which miR-7a-1 is embedded *(Hnrnpk*), and
129 from which the most abundant miR-7 primary transcript is generated (Supplementary Table S2).
130 Taken together these data show that OGD specifically regulates miR-7a-5p variant at the
131 transcriptional and/or post-transcriptional level.
132
133 To test the possible functional relevance of the upregulation of miR-7a-5p, we acquired predicted and
134 validated targets of miR-7a-5p using *miRWalk* algorithm analysis[33,34] and compared their overall

135 expression in conditions of OGD. In accordance with the upregulation of miR-7, miR-7 targets
136 showed a significant overall downregulation (Figure 2F, Supplementary Table S4, Supplementary
137 Figure S2B), suggesting a canonical functional repressive role of this miRNA.
138 The role of miR-7 interaction with ciRS-7 remains controversial, and it is thought to set the balance
139 between a positive and negative feedback[8,9] (Figure 2A). Additionally, Cyrano promotes target-
140 directed miRNA degradation (TDMD) of miR-7 through a site of almost perfect complementarity,
141 indirectly regulating ciRS-7 levels and localization[8] (Figure 2A). In our dataset the lncRNA Cyrano
142 was significantly downregulated upon OGD (Figure 2G), in line with the observed upregulation in
143 miR-7a-5p (Figure 2B). To identify a first responder to OGD in the context of this molecular circuitry
144 we evaluate the time-dependent changes in the levels of these molecules. We subjected cortical
145 neurons to OGD for 1, 6, 12 and 24 hours and assessed the expression level of ciRS-7, miR-7 and
146 Cyrano. We detected a significant downregulation of ciRS-7 and Cyrano already at 6 hours after
147 OGD, prior to the upregulation of miR-7 at 12 hours (Figure 2H). Interestingly, our data revealed a
148 significant downregulation of miR-7 at 6h of OGD concomitantly with downregulation in ciRS-7 and
149 Cyrano, which is in line with the previously suggested role of ciRS-7 in stabilizing miR-7[9].

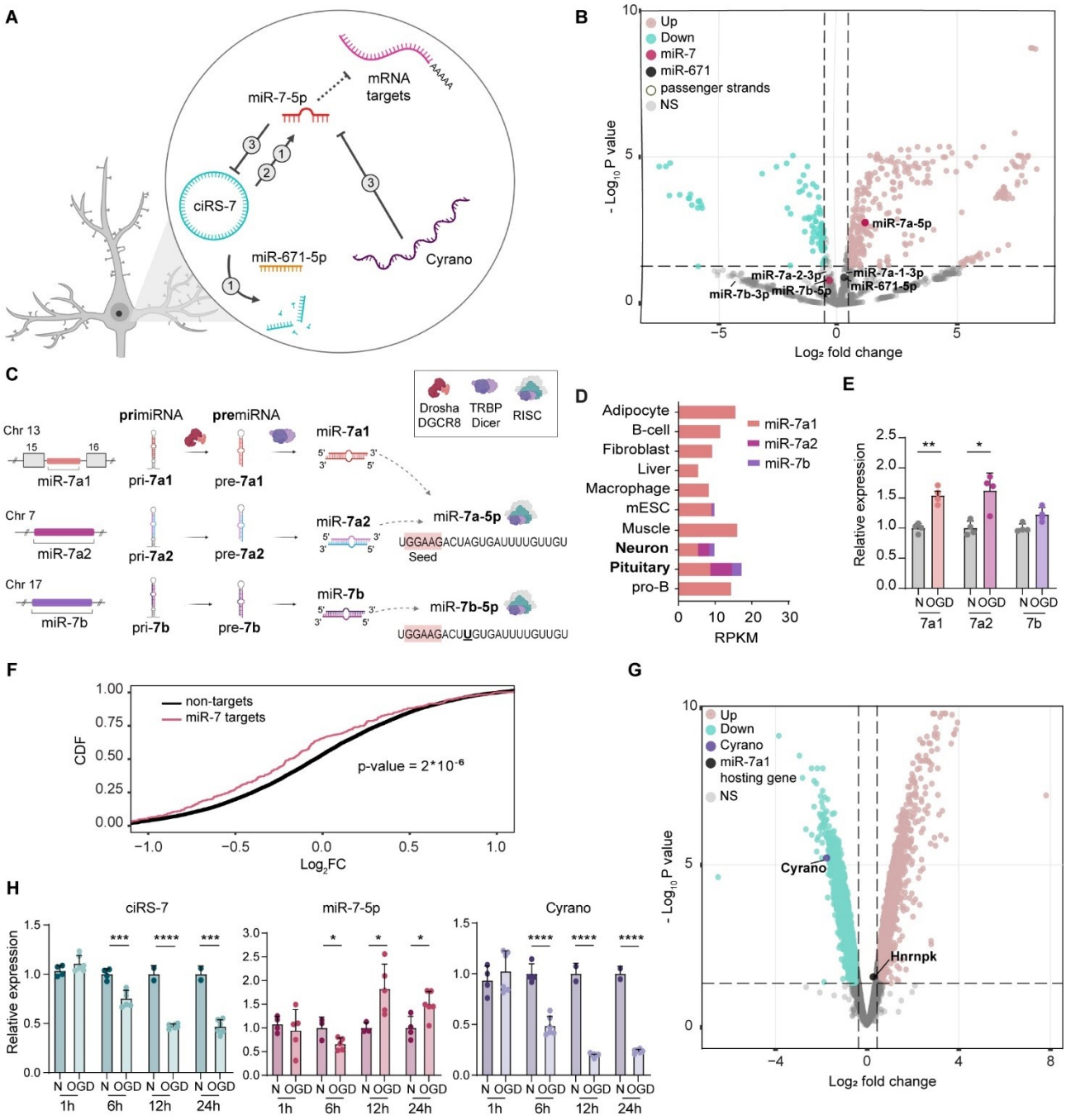

Figure 2. ciRS-7 network is dynamically altered in ischemic stroke like conditions.

(A) Schematic of the regulatory network involving ciRS-7, miR-7, Cyrano, and miR-671. References: (1) Hansen et al., EMBO J, 2011; Hansen et al., Nature, 2013; (2) Piwecka et al., Science, 2017; (3) Kleaveland et al., Cell, 2018. **(B)** Volcano plot of differentially expressed microRNAs in OGD-treated cortical neuron cultures. Significantly upregulated (pink) and downregulated (green) microRNAs, miR-7 variants (red), miR-7 passenger strands (white), and miR-671 (black) are

157 highlighted (n = 5; p-adj. < 0.05 and |log2FC| > 0.3). **(C)** Schematic of murine genomic loci
158 illustrating the transcription of miR-7 primary transcripts (pri-miR), their processing into precursor
159 molecules (pre-miR), and maturation into mature miR-7. The shared seed sequence between miR-7a-
160 5p and miR-7b-5p is highlighted in red, and the non-seed mismatch at position 10 between the
161 variants is underlined in black. **(D)** Bar plot of miR-7 loci reads per kilobase million (RPKM) in
162 different cell type obtained from GRO-seq datasets. **(E)** Bar plot of miR-7 pri-miRNA expression in
163 cortical neurons post-OGD treatment quantified by qPCR. Relative expression normalized to
164 normoxic condition (n = 4; * p < 0.05, ** p < 0.01, paired t-test; mean ± SD).**(F)** Cumulative
165 distribution functions (CDFs) plot of log fold changes of genes in OGD-treated wild-type cortical
166 neurons (12h) compared to normoxic conditions. Red curve represents CDF for miR-7 targets, and
167 black curve for non-targets (n = 5; p-value from Kolmogorov-Smirnov test). **(G)** Volcano plot of
168 differentially expressed transcripts in OGD-treated cortical neuron cultures. Significantly upregulated
169 (pink) and downregulated (green) transcripts, Cyrano (purple), and miR-7 hosting gene HnrnpK
170 (black) are highlighted (n = 5; p-adj. < 0.05 and |log2FC| > 0.3). **(H)** Bar plot of ciRS-7 (blue), miR-
171 7 (magenta), and Cyrano (purple) quantification by qPCR in OGD-treated cortical neurons at various
172 timepoints (1h, 6h, 12h, and 24h). Relative expression normalized to normoxic condition (normoxia
173 n = 2-4, OGD n = 5-6; * p < 0.05, *** p < 0.001, **** p < 0.0001, unpaired t-test; mean ± SD).
174
175

176 ***ciRS-7 KO neurons exhibit a distinct outcome after OGD without altering the overall OGD***
177 ***response***

178 The absence of ciRS-7 alters synaptic transmission in excitatory neurons and produces schizophrenia-
179 like phenotype *in vivo*[9], connecting this molecule to glutamatergic transmission. This is of particular
180 interest in conditions of ischemic stroke, where glutamate mediated excitotoxicity is a critical
181 contributor to neuronal cell death[12]. Our cortical neuron culture enriched in glutamatergic neurons

182 (Figure 1B) provides a system in which these events can be studied *in vitro.* Neurons cultured from
183 ciRS-7 KO mice showed higher Ca^{2+}-responses to the stimulation with glutamate compared to their
184 wild-type (WT) counterparts (Figure 3A). Consequently, ciRS-7 KO neurons also exhibited a
185 significantly higher sensitivity to excitotoxicity upon exposure to high concentration of glutamate
186 (Figure 3B).
187
188 To test if this increased sensitivity to glutamate is affecting gene expression changes in OGD, we
189 subjected the ciRS-7 KO cortical cultures to OGD for 12 hours, following the previous experimental
190 design (Supplementary Figure S1A) and performed total RNA-seq. OGD induced deregulation in
191 total of 5767 genes in ciRS-7 KO neurons compared to normoxic conditions, of which the 85% were
192 shared with WT neurons (Figure 3C, Supplementary Table S5). Consistent with this, the analysis of
193 interaction terms in the differential expression analysis, aimed at distinguishing differences in the
194 OGD response between WT and ciRS-7 KO, revealed no significant difference in the overall OGD
195 response between the two genotypes (Supplementary Table S6). However, 871 genes were
196 differentially expressed only in ciRS-7 KO neurons, while the expression of 1260 genes was
197 exclusively altered in WT neurons subjected to OGD. ciRS-7 WT specific genes altered in OGD were
198 functionally enriched in mitochondrial processes, DNA metabolism, regulation of cell-cycle and
199 oxidative stress-induced apoptosis (Figure 3D). The 871 KO-specific genes were instead involved in
200 developmental and pro-regenerative processes (*progenitor migration to the cortex, DNA replication,*
201 *transcription, cerebellar cortex development*) (Figure 3E). Despite the genetic predisposition to
202 glutamate sensitivity of the ciRS-7 KO, which would suggest a deleterious outcome in the response
203 to OGD, ciRS-7 KO neurons regulate pathways of resilience during OGD. In support of this, ciRS-7
204 KO neurons did not show increased cell death compared to WT in response of OGD treatment
205 (Supplementary Figure S2C). This result implies a distinction in OGD outcome not attributed to a

206 change in the OGD response itself, but rather to the regulation of the cascade of processes downstream
207 of the response.
208 Interestingly, the lack of ciRS-7 did not affect OGD induced changes in the expression of miR-7 and
209 Cyrano (Figure 3F). Similar to WT neurons, Cyrano lncRNA was downregulated in ciRS-7 KO
210 neurons responding to OGD (Figure 3F, Supplementary Table S5). Moreover, even though ciRS-7
211 KO neurons stably express lower levels of miR-7a-5p[9] (Figure 3F, Supplementary Table S5), small-
212 RNA sequencing revealed a significant upregulation of miR-7a-5p in response to OGD also in these
213 neurons (Figure 3F, Supplementary Table S5). In line with our previous findings, we detected no
214 changes in miR-671-5p, miR-7b-5p and miR-7 passenger strand expression (Supplementary Table
215 S5). Nonetheless, whilst the expression in miR-7a-5p in OGD remained lower in ciRS-7 KO neurons
216 compared to WT neurons (Figure 3F), the targets of miR-7a-5p, both predicted and validated, showed
217 a significant global repression in these conditions (Figure 3G).

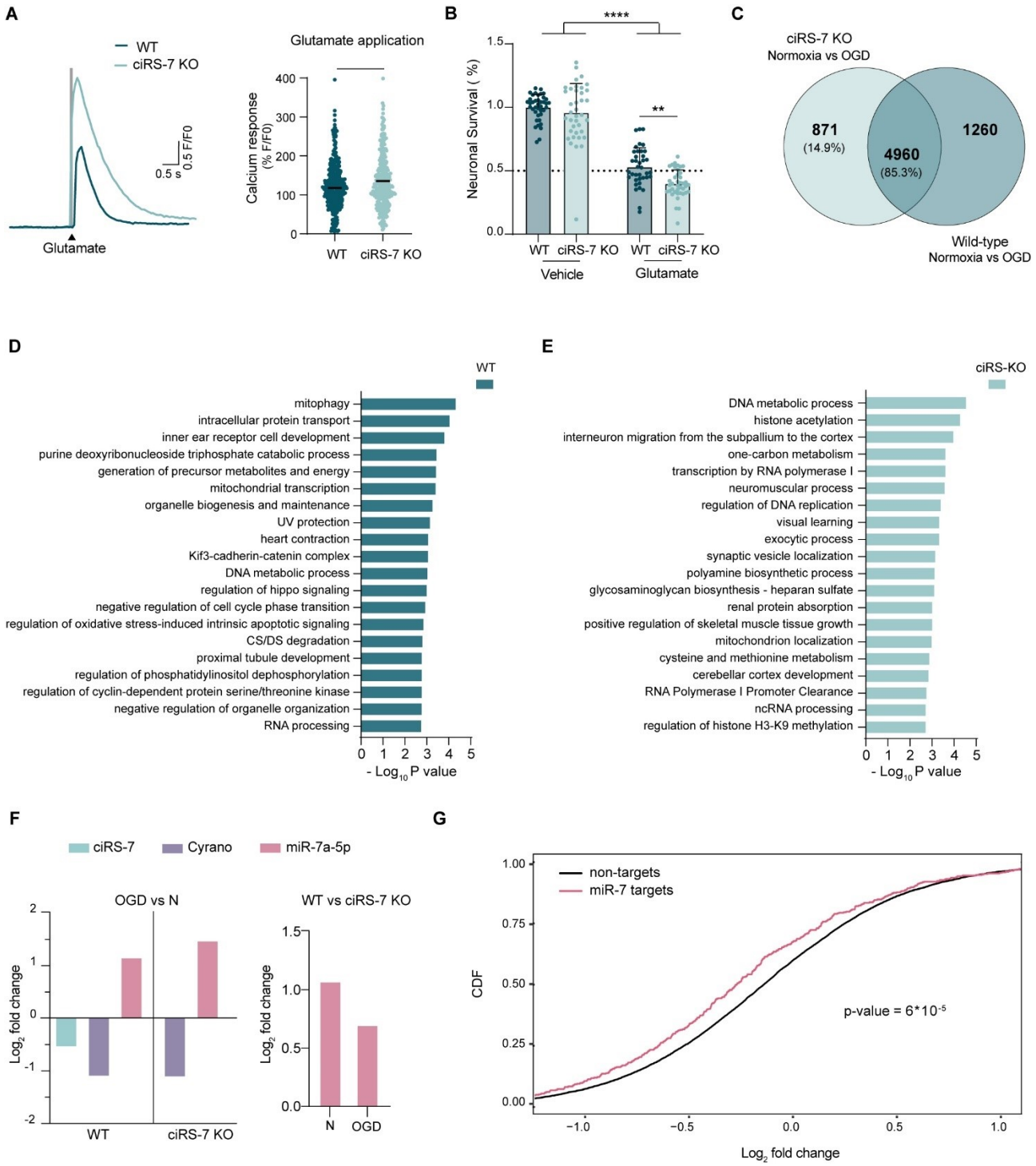

Figure 3. ciRS-7 KO genotype exhibits differential OGD phenotypical output without affecting the OGD induced changes in miR-7 and Cyrano. (A) (Left) Representative trace of calcium-induced fluorescence in response to glutamate treatment in wild-type and ciRS-7 KO cortical neurons. (Right) Scatter dot plot of calcium imaging analysis showing the cellular response to glutamate in wild-type and ciRS-7 KO cortical neurons (n = 8; * $p < 0.05$, unpaired t-test; central bar represents

median value). **(B)** Bar plot of relative absorbance in MTT viability assay for wild-type and ciRS-7 KO cortical neurons treated with vehicle or 250μM glutamate. Data presented as survival % normalized to wild-type vehicle (n = 4; * $p < 0.05$, **** $p < 0.0001$, one-way ANOVA corrected with Tukey's post-hoc test; mean ± SD). **(C)** Venn diagram of differentially expressed genes in normoxic versus OGD conditions of wild-type and ciRS-7 KO cortical neurons (n = 5; p-adj. < 0.05 and |log2FC| > 0.3). **(D)** Bar plot of functional enrichment analysis top 20 significant Metascape clusters performed on differentially expressed genes in wild-type normoxic versus OGD cortical neurons. **(E)** Bar plot of top 20 significant Metascape clusters from functional enrichment analysis on differentially expressed genes in wild-type normoxic versus OGD cortical neurons. **(F)** (Left) Bar plot of log2FC for ciRS-7 (blue), miR-7 (magenta), and Cyrano (purple) from RNA-seq of wild-type and ciRS-7 KO cortical neurons in normoxic conditions versus after 12h of OGD treatment. (Right) Bar plot of log2FC for miR-7 (magenta) from RNA-seq, highlighting expression differences in normoxic conditions (N) or OGD between wild-type and ciRS-7 KO genotypes (n = 5; p-adj. < 0.05 and |log2FC| > 0.3). **(G)** Cumulative distribution functions (CDFs) plot of log fold changes of genes in OGD-treated ciRS-7 KO cortical neurons (12h) compared to normoxic conditions. The red curve represents CDF for miR-7 targets, while the black curve represents non-targets (n = 5; p-value from Kolmogorov-Smirnov test).

247 ***Alteration of ciRS-7 affects ischemic stroke outcome in vivo***

248 To assess the reproducibility of our findings in ischemic stroke *in vivo*, *BALB/c* mice were subjected
249 to permanent middle cerebral artery occlusion (pMCAO) and levels of ciRS-7, Cyrano and miR-7a-
250 5p were evaluated by qPCR at six hours, one day and five days post-ischemia. In line with our *in*
251 *vitro* results, we detected a significant downregulation of ciRS-7 and Cyrano and upregulation of
252 miR-7a-5p in the peri-ischemic cortex (PI) at one day post-ischemia (dpi) compared to contralateral
253 cortex (CL) (Figure 4A). Moreover, similar to OGD, we failed to detect alterations in miR-671-5p
254 levels (Supplementary Figure S2D).

255

256 To explore the functional implications of ciRS-7 KO neurons ambiguous behavior involving
257 glutamate sensitivity without increased cell death during OGD, we tested whether ciRS-7 KO mice
258 exposed to transient ischemic stroke would show altered vulnerability to ischemic damage and
259 associated sensorimotor impairments. The ischemic lesion size was measured using Magnetic
260 Resonance Imaging (MRI) and behavioral deficits were assessed using Neurological Severity Scores
261 (NSS) at acute (1dpi), subacute (3dpi) and chronic (7dpi) timepoints after transient middle cerebral
262 artery occlusion (tMCAO) (Figure 4B). At 1dpi, ciRS-7 KO mice showed a significant reduction in
263 the ischemic lesion volume compared to their WT controls (Figure 4C) and significantly ameliorated
264 motor deficits (Figure 4D). Interestingly, ciRS-7 KO animals lesion size changes occurred transiently
265 at the acute timepoint (1dpi), without delaying damage progression (Supplementary Figure S4A,B).
266 To identify the molecular changes associated with acute reduction in the lesion size and motor deficits
267 in ciRS-7 KO mice, mice were sacrificed at 1dpi and peri-ischemic and the contralateral cortex was
268 used for mRNA sequencing. IPA analysis of differentially expressed genes in the peri-ischemic cortex
269 of ciRS-7 KO animals indicated substantial inhibition in pathways related to neuronal and tissue
270 damage, cytokine and interleukin release, and calcium influx compared to WT controls (Figure 4E,
271 Supplementary Table S7). Moreover, most differentially expressed genes were mostly contributing

272 to pathways of *necrosis* (205 genes) and *quantity of cytokine* (41 genes), suggesting that the decreased
273 lesion size in the ciRS-7 KO mice may be due to inhibition of necrotic pathways and reduction in
274 cytokine release.
275 Aiming to identify crucial cellular responders mediating the observed gene expression changes, we
276 carried out deconvolution analysis by using adult mouse brain scRNA-seq data[35] to assess the
277 contribution of different cell populations in our bulk mRNA sequencing dataset. This analysis
278 identified neurons and astrocytes as major cellular responders contributing to WT and ciRS-7 KO
279 gene expression profiles (Figure 4F). In line with the significantly reduced tissue death measured by
280 MRI (Figure 4C), ciRS-7 KO mice exhibited increased neuronal involvement in the peri-infarct
281 cortex compared to WT mice, accompanied by a decrease in astrocyte contribution. To confirm this,
282 brain slices from ischemic ciRS-7 KO mice were collected at the peak of the immune response (7dpi)
283 [36] and stained for astrocytic glial fibrillary acidic protein (GFAP). Although ischemic stroke induced
284 GFAP expression in the peri-infarct cortex for both WT and ciRS-7 KO mice, ciRS-7 KO mice
285 exhibited significantly reduced astrogliosis compared to WT animals (Figure 4G).
286 At molecular level, tMCAO significantly downregulated ciRS-7 in WT mice at 1dpi in the peri-
287 ischemic cortex, while miR-7-5p and Cyrano levels remained unaltered (Figure 4H, Supplementary
288 Figure S4C). However, ciRS-7 KO mice showed a significant upregulation of miR-7-5p and unaltered
289 Cyrano levels (Figure 4H). These data suggest a correlation between the absence of ciRS-7 and a
290 faster upregulation of miR-7 in response to transient ischemic stroke and a marginal role of Cyrano
291 in this system at this timepoint.

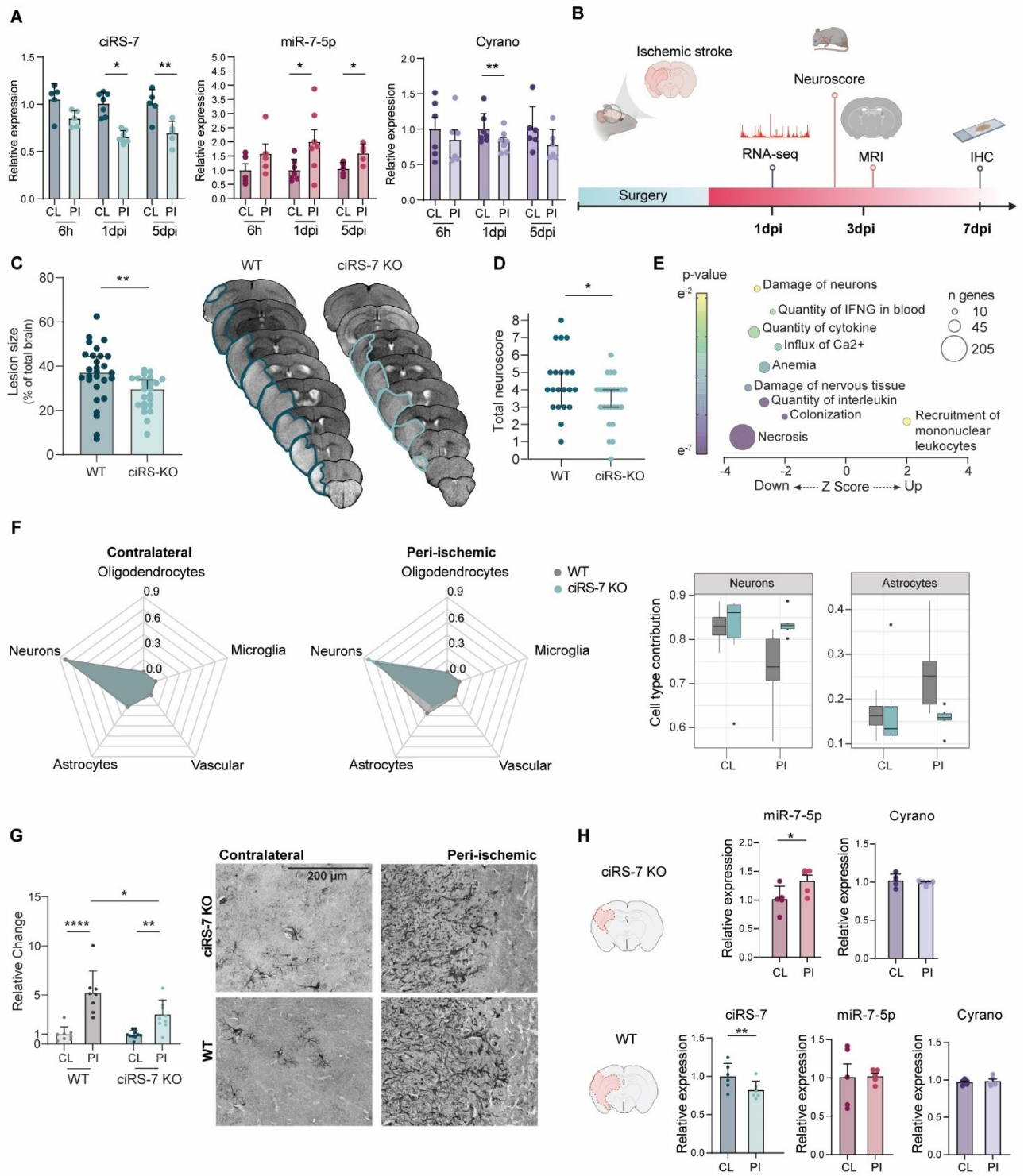

292

293 **Figure 4. Lack of ciRS-7 ameliorates ischemic stroke outcome in vivo.**

294 **(A)** Bar plot of qPCR quantification for ciRS-7 (blue), miR-7 (magenta), and Cyrano (purple) in 3-4

295 months old BALB/c mice after pMCAo surgery. Peri-ischemic (PI) and contralateral (CL) cortices

296 were collected at different timepoints (6h, 1d, and 5d). Relative expression normalized to the average

297 CL expression (n = 6-7; * $p < 0.05$, *** $p < 0.001$, **** $p < 0.0001$, paired t-test; mean ± SD). **(B)**
298 Schematic of the experimental design: Wild-type and ciRS-7 KO mice underwent tMCAO surgery,
299 followed by neuroscore testing and MRI monitoring at 1, 3, and 7 days post-surgery (dpi). At 1dpi,
300 six mice were utilized to obtain peri-ischemic and contralateral cortices for RNA-sequencing.
301 Immunohistochemistry analysis was performed at later timepoints using eight to nine mice per group.
302 **(C)** (Left) Bar plot of MRI quantification of the lesion size in wild-type and ciRS-7 KO mice 1 day
303 post-tMCAO surgery. Data presented as lesion percentage on total brain size adjusted for edema (n =
304 25-28 per group; ** $p < 0.01$, Mann–Whitney test; median with 95% confidence interval). (Right)
305 Representative MRI image illustrating changes in lesion perimeter (blue) between wild-type (WT)
306 and ciRS-7 KO animals. **(D)** Scatter dot plot of sensorimotor deficits assessed by neuroscore in
307 tMCAO wild-type and ciRS-7 KO mice at 1dpi. Data presented as total neuroscore (n = 22-25 per
308 group; * $p < 0.05$, Mann–Whitney test; median with 95% confidence interval). **(E)** Bubble plot of
309 Ingenuity Pathway Analysis (IPA) for differentially expressed genes between wild-type and ciRS-7
310 KO peri-ischemic cortices from RNA-seq. Z-score reflects IPA prediction of pathway activation
311 (positive) or inhibition (negative) in ciRS-7 KO. Color bar indicates p-value significance (yellow to
312 purple), and bubble size represents the number of genes in the pathway ($|z| > 2$ considered significant;
313 pathways with >10 genes included). **(F)** (Left) Spiderweb plot of bulk RNA-seq deconvolution scores
314 of wild-type (gray) and ciRS-7 KO (blue) contralateral and peri-ischemic cortices. (Right) Bar plot
315 illustrating neurons and astrocyte contributions based on deconvolution scores in wild-type (gray)
316 and ciRS-7 KO (blue) contralateral and peri-ischemic regions. **(G)** (Left) Bar plot of quantification
317 for GFAP DAB (3,3′-Diaminobenzidine) immunostaining in wild-type and ciRS-7 KO tMCAO mice
318 at 7dpi. (Right) Representative images of the staining highlighting $GFAP^+$ cells. Relative expression
319 normalized to the average contralateral expression of wild-type mice (n = 8; * $p < 0.05$, ** $p < 0.01$,
320 **** $p < 0.0001$, one-way ANOVA corrected with Tukey's post-hoc test; mean ± SD). **(H)** Bar plot
321 of qPCR quantification for ciRS-7 (blue), miR-7 (magenta), and Cyrano (purple) in contralateral (CL)

322 and peri-ischemic (PI) cortices of ischemic wild-type and ciRS-7 KO mice at 1dpi. Schematic
323 representation correlates with MRI lesion size at the same timepoint. Data normalized to the average
324 contralateral expression of wild-type mice (n = 5 per group; * $p < 0.05$, ** $p < 0.01$, paired t-test;
325 mean ± SD).
326

327 ***ciRS-7 prevents miR-7 effects on dampening glutamatergic signaling in excitatory neurons***
328 Previous studies linked miR-7 to oxidative stress response[37], in particular in low glucose conditions[38].
329 To establish the possible functional link between the upregulation of miR-7 in ciRS-7 KO mice in
330 conditions of ischemic stroke, we subjected cre-loxP inducible miR-7 KO mice[39] to tMCAO (Figure
331 5A, Supplementary Figure S5A,B). At the acute timepoint (1dpi), no changes in lesion volume, as
332 measured by MRI, were detected between miR-7 KO and WT mice (Supplementary Figure S5C).
333 Accordingly, miR-7 KO mice did not show any differences in motor deficits compared to their WT
334 controls (Supplementary Figure S5D). However, miR-7 KO mice (Figure 5B) exhibited an increase
335 in the lesion volume compared to their WT controls at later timepoint (7 dpi), unrelated to changes in
336 Neuroscore (Supplementary Figure S5E), indicating a potential role of miR-7 in regulating ischemia-
337 induced secondary cell death.
338

339 To understand the functional role of miR-7 in ischemic stroke, we first validated miR-7 functional
340 target sites in our system by analyzing miR-7 target binding sites in an Ago2 HITS-CLIP sequencing
341 dataset of pyramidal excitatory neurons[40] (Figure 5C, Supplementary Table S8). By identifying
342 RISC-associated binding sites on expressed transcripts in mature pyramidal neurons, our analysis of
343 the minimal seed site hexamer of miR-7 revealed 645 potential targets in the 3' UTRs (Figure 5D).
344 As expected, ciRS-7 had the highest number of functional binding sites (n=139), representing over
345 11% of the total reads (Supplementary Table S8). The intersection of Ago2 HITS-CLIP physical
346 targets and the downregulated genes in the peri-ischemic cortex of ciRS-7 KO mice, where miR-7 is

347 upregulated, highlighted 276 common genes (Figure 5E). These genes were functionally enriched in
348 pathways related to glutamatergic synaptic transmission and morphological changes of neuronal
349 projections (Figure 5F, Supplementary Figure S6).
350
351 To discern the specific contributions of ciRS-7 and miR-7 to glutamatergic signaling and neuronal
352 morphological changes, we opted to replicate the molecular changes associated with low ciRS-7 and
353 high miR-7 *in vitro.* We transduced ciRS-7 WT and KO neurons with lentivirus overexpressing GFP
354 and miR-7a or GFP only, under the neuronal specific human Synapsin 1 (hSYN) promoter. Infection
355 efficiency was evaluated through fluorescence microscopy (Supplementary Figure S7A) and we
356 confirmed by RT-qPCR that miR-7a-5p levels resembled the endogenous levels under OGD
357 condition (Supplementary Figure S7B). Whilst overexpression of miR-7 in WT neurons did not affect
358 the overall neuronal glutamate excitability, increased levels of miR-7 in ciRS-7 KO neurons
359 significantly reduced their response to glutamate (Figure 5G), thus reverting the genotype of
360 glutamate sensibility of the ciRS-7 KO neurons. This appeared to be a glutamate specific effect, as
361 the overexpression of miR-7 did not affect GABAergic response (Supplementary Figure S7C).
362
363 Finally, to evaluate the functional impact of the potential targets of miR-7 involved in morphological
364 changes of neuronal projections (Figure 5F), we performed live imaging analysis of neurite outgrowth
365 of ciRS-7 KO and WT neurons infected with miR-7 lentivirus. In agreement with the calcium imaging
366 experiment, we were able to detect a significant increase in the neurite length when over expressing
367 miR-7 in ciRS-7 KO cells, but not in WT neurons (Figure 5H). This aligns with a previous study
368 showing a direct impact of miR-7 overexpression on neurite length in a neuroblastoma cell line[41].
369 Considering circRNAs are typically low in cell lines due to their rapid proliferation[42], we questioned
370 whether the effect of miR-7 on neurite length was due to the absence of ciRS-7 interference.
371

However, circRNAs are known to be poorly expressed in cell lines due of their high proliferation rate[42]. So, we wondered whether this miR-7 direct effect on neurite length was due to lack of ciRS-7 interference. We confirmed that the murine neuroblastoma cell line N2A expresses negligible ciRS-7 levels even when differentiated with retinoid acid, despite higher levels of Cyrano and miR-7 (Supplementary Figure S8A,B,C).

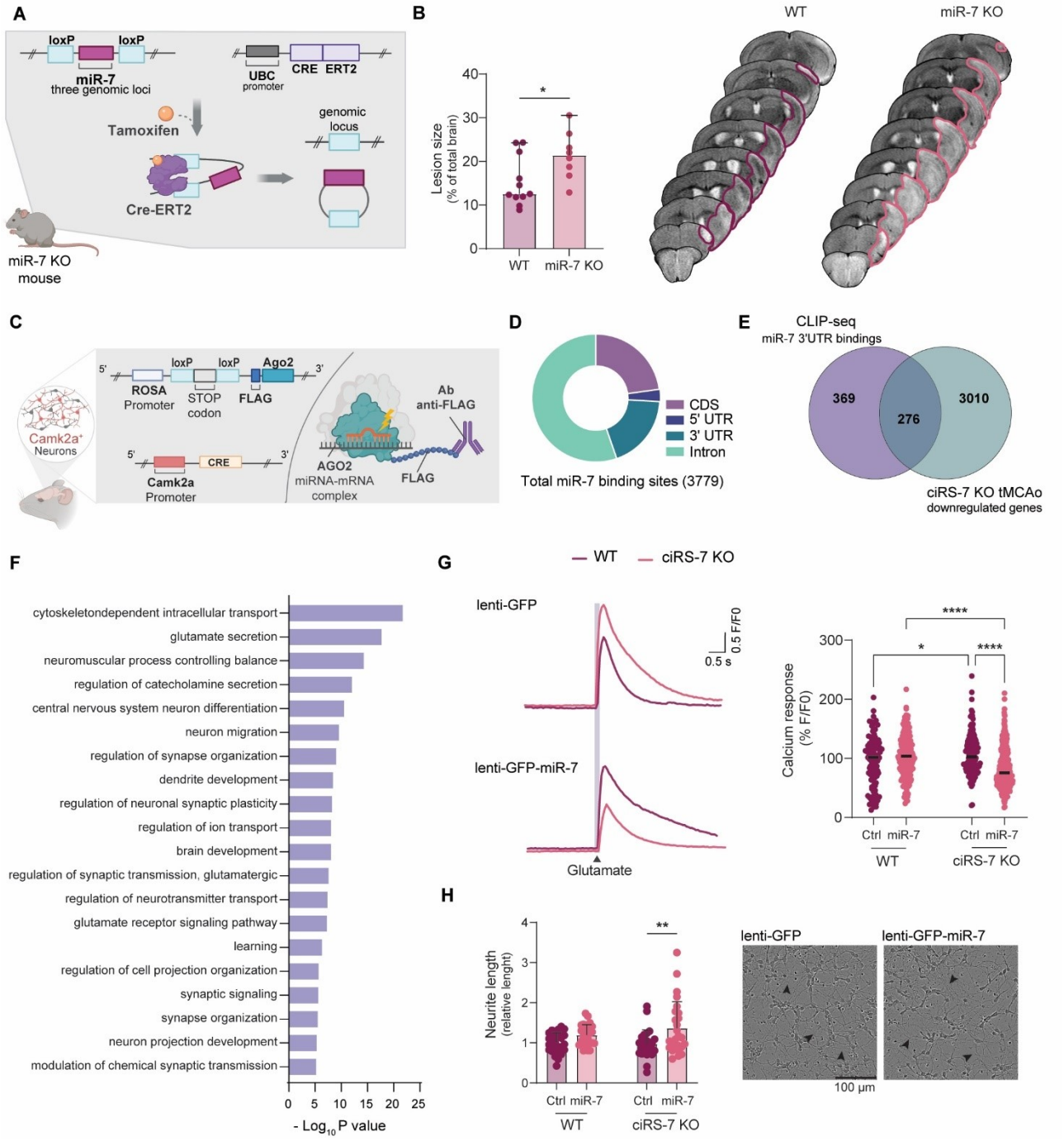

378 **Figure 5. Lack of miR-7 exaggerates ischemic stroke outcome regulating glutamatergic**
379 **response.**
380 **(A)** Schematic of Cre-LoxP miR-7 KO animal model: mice have a transgenic genome with LoxP
381 sequences (blue) flanking all three miR-7 loci (magenta), and tamoxifen (orange)-inducible Cre
382 recombinase (purple). Tamoxifen activation of Cre recombinase leads to miR-7 loci deletion. Control
383 mice lack the Cre recombinase transgene. **(B)** (Left) Bar plot of MRI quantification for lesion size in
384 wild-type and miR-7 KO mice one day post-tMCAO surgery. Data presented as lesion percentage on
385 total brain size adjusted for edema ($n = 8$-11 per group; * $p < 0.05$, Mann–Whitney test; median with
386 95% confidence interval). (Right) Representative MRI image illustrating changes in lesion perimeter
387 (blue) between wild-type (WT) and miR-7 KO animals. **(C)** Schematic of recombinant mice for
388 generating Ago2 CLIP-seq data in excitatory neurons: FLAG-Ago2 (blue) is selectively translated in
389 Cam2Ka$^+$ (red) excitatory neurons, where Cre recombinase (yellow) expression removes a stop codon
390 (gray) leading to FLAG-Ago2 translation. Following cross-linking (thunder), the FLAG-Ago2-
391 miRNA-target complex is immunoprecipitated with an anti-FLAG antibody (purple), and the
392 sequenced output represents the miRNA-target complex. **(D)** Pie chart illustrating the distribution of
393 miR-7 binding sites from CLIP-seq analysis. Among the 3779 identified binding sites, categories
394 include protein coding sequences (CDS, purple), 5' untranslated regions (5' UTR, blue), 3'
395 untranslated regions (3' UTR, dark green), and intronic sequences (Intron, light green). **(E)** Venn
396 diagram depicting the miR-7 binding sites in the 3' UTR identified by CLIP-seq in excitatory neurons
397 (645) and the downregulated genes in the peri-ischemic region of ciRS-7 KO tMCAO animals (3286),
398 where miR-7 is upregulated. The overlap (276 genes) represents potential miR-7 physical targets
399 affected in ischemic stroke. **(F)** Bar plot of the top 20 significant Metascape clusters from functional
400 enrichment analysis on genes identified as miR-7 physical targets potentially affected in ischemic
401 stroke. **(G)** (Left) Representative trace of calcium-induced fluorescence in response to glutamate
402 treatment in wild-type and ciRS-7 KO neurons infected with miR-7 or control lentivirus. (Right)

403 Scatter dot plot of calcium imaging analysis quantifying the cellular response to glutamate in wild-
404 type and ciRS-7 KO cortical neurons infected with control (GFP) or miR-7 overexpressing (GFP +
405 miR-7) virus (n = 5; * $p < 0.05$, **** $p < 0.0001$, Kruskal–Wallis test; central bar represents median
406 value). **(H)** (Left) Bar plot of neurite length quantified through live imaging of wild-type and ciRS-7
407 KO cortical neurons infected with control (GFP) or miR-7 overexpressing lentivirus (GFP + miR-7).
408 Data normalized to the average neurite length of wild-type GFP-infected neurons (n = 3 biological
409 replicates, n = 8 technical replicates; ** $p < 0.01$, one-way ANOVA test corrected with Tukey's post-
410 hoc test; mean ± SD). (Right) Representative image of ciRS-7 KO cortical neurons infected with
411 control (GFP) or miR-7 overexpressing virus (GFP + miR-7).
412
413 ***miR-7 modulates AMPA-mediated glutamatergic signaling via ciRS-7/Cyrano network in ischemic***
414 ***conditions***
415 To further unravel the intricate interactions within the miR-7/ciRS-7/Cyrano network, we conducted
416 gain and loss of function experiments to modulate miR-7 expression in the context of ischemic stroke.
417 We utilized a lentivirus expressing the Cyrano CR1 region, known for its role in mediating miR-7
418 degradation through TDMD[8]. Wild-type cortical neurons were transduced with lentivirus carrying
419 CR1 or a control region featuring a mutated miR-7 binding site before exposure to a 12-hour period
420 of OGD. As expected, overexpression of Cyrano CR1 region led to a decrease in miR-7 expression
421 in normoxic conditions. Additionally, it prevented the OGD-induced increase in miR-7, in stark
422 contrast to the mutated CR1, which had no impact on OGD-induced upregulation of miR-7 (Fig. 6A).
423 Remarkably, preventing the increase in miR-7 expression preserved the levels of ciRS-7 during OGD,
424 disclosing a previously proposed antagonistic relationship between these molecules[8]. The
425 overexpression of the synthetic construct had no influence on the OGD-induced downregulation of
426 the endogenous full-length Cyrano. Conversely, lentiviral induced overexpression of miR-7 induced
427 an amplified miR-7 response during OGD (Fig. 6B). This molecular phenotype was consistently

428 associated with a downregulation of ciRS-7, even under physiological conditions, further suggesting
429 a potential involvement of miR-7 expression in the downregulation of ciRS-7. As expected, miR-7
430 overexpression had no effect on Cyrano basal expression or OGD-induced Cyrano downregulation
431 (Fig. 6B).
432 By leveraging miR-7 targets validated through CLIP-seq that were dysregulated in ischemic mice
433 (Fig. 5E, Supplementary Table S7), we pinpointed Gria1, a gene encoding a subunit of the AMPA
434 receptor, critical for mediating glutamate excitotoxicity in ischemic stroke pathophysiology[43]. The 3'
435 UTR of Gria1 contains two potential 6mer binding sites for miR-7a-5p (Fig. 6C). To validate the
436 physical interaction of these binding sites with miR-7a, we co-expressed a luciferase vector
437 containing the 3' UTR of Gria1 and miR-7a-5p in the HEK293T cell line. We observed a significant
438 post-transcriptional canonical effect of miR-7 on the 3'UTR which was absent with an unrelated
439 control miRNA (Fig. 6C). To further confirm the significance of this relationship in conditions of
440 ischemic stroke, we measured the levels of Gria1 in cortical neurons transduced with miR-7 lentivirus
441 prior OGD for 12h. In line with the RNA-seq data (Supplementary Figure S2B), OGD treatment led
442 to a decrease in Gria1 expression in neurons transduced with the control vector. However,
443 overexpression of miR-7 resulted in a 50% reduction in Gria1 mRNA levels under normal oxygen
444 conditions, with no further alterations during OGD (Fig 6D). Overexpression of Cyrano CR1 region
445 in neurons subjected to OGD prevented the OGD-induced downregulation of Gria1 (Fig. 6E). To
446 demonstrate that the miR-7-mediated effect on Gria1 lead to a decrease response to AMPA, we
447 carried out calcium imaging in ciRS-7 KO neurons that were lentivirally transduced to overexpress
448 miR-7. In these conditions, ciRS-7 buffering effect on miR-7 is disrupted. As expected, the
449 upregulation of miR-7 had no impact on wild-type neurons. However, in ciRS-7 KO neurons, we
450 observed a significant decrease in AMPA-induced Ca^{2+} responses in miR-7 overexpressing neurons
451 (Fig. 6F). This finding reinforces the link between miR-7 and glutamatergic signaling, indicating that

the diminished glutamatergic response attributed to miR-7 is, to some extent, a result of suppression of AMPA signaling achieved through the downregulation of Gria1.

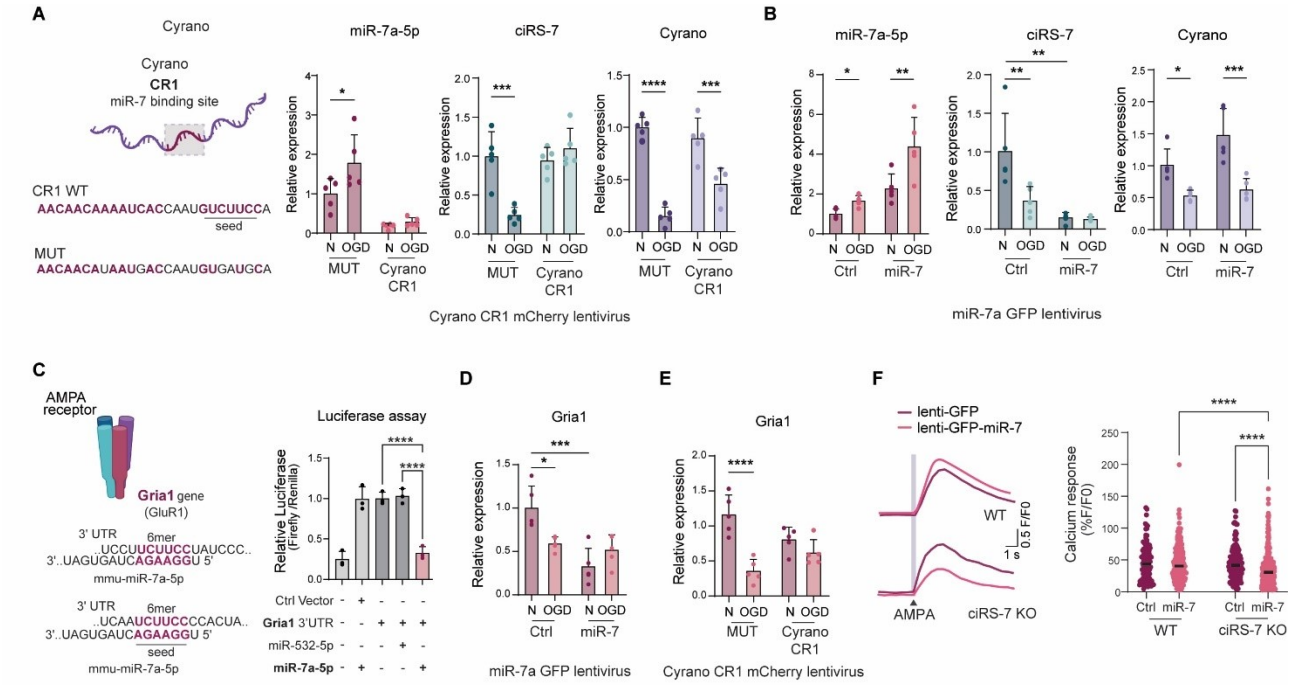

Figure 6. miR-7 regulation in OGD depends on ciRS-7 and Cyrano and modulate AMPA response. (A) (Left) Schematic of the wild-type Cyrano CR1 region (CR1) and its miR-7 binding sites mutated version (MUT). Magenta indicates pairing with miR-7a-5p, encompassing both seed region and a more extensive one. (Right) Bar plot of qPCR quantification for miR-7 (magenta), ciRS-7 (blue), and Cyrano (purple) in cortical neurons overexpressing Cyrano CR1 region (Cyrano CR1) or its mutated version (MUT) along with mCherry, treated with OGD for 12 hours. Relative expression normalized to normoxic condition of the mutated lentivirus (n = 5; * $p < 0.05$, *** $p < 0.001$, **** $p < 0.0001$, one-way ANOVA corrected with Tukey's post-hoc test; mean ± SD). **(B)** Bar plot of qPCR quantification for miR-7 (magenta), ciRS-7 (blue), and Cyrano (purple) in cortical neurons overexpressing miR-7 GFP or a control vector with only GFP (Ctrl), treated with OGD for 12 hours. Relative expression normalized to normoxic condition of the control lentivirus (n = 5; * $p < 0.05$, ** $p < 0.01$, *** $p < 0.001$, one-way ANOVA corrected with Tukey's post-hoc test; mean ± SD). **(C)** (Left) Schematic of the heteromeric AMPA receptor with its four subunits highlighted in

468 different colors. Gria1, encoding the GluR1 subunit, is highlighted in magenta. Two 6mer sites on
469 Gria1 3' UTR and their potential pairing with miR-7a-5p in the seed region are shown (underlined).
470 (Right) Bar plot of luciferase assay fluorescence quantification in HEKT293 cells transfected with
471 control vector (Ctrl vector), Gria1 3' UTR, and miR-532-5p (lacking binding sites) or miR-7a-5p
472 (magenta). Relative expression normalized to Gria1 3' UTR vector alone (n = 3; **** $p < 0.0001$,
473 one-way ANOVA corrected with Tukey's post-hoc test; mean ± SD). **(D)** Bar plot of qPCR
474 quantification for Gria1 (magenta) in cortical neurons overexpressing miR-7 GFP or a control vector
475 with only GFP (Ctrl), treated with OGD for 12 hours. Relative expression normalized to normoxic
476 condition of the control lentivirus (n = 5; * $p < 0.05$, *** $p < 0.001$, one-way ANOVA corrected with
477 Tukey's post-hoc test; mean ± SD). **(E)** Bar plot of qPCR quantification for Gria1 (magenta) in
478 cortical neurons overexpressing Cyrano CR1 region (Cyrano CR1) or its mutated version (MUT)
479 along with mCherry, treated with OGD for 12 hours. Relative expression normalized to normoxic
480 condition of the mutated lentivirus (n = 5; **** $p < 0.0001$, one-way ANOVA corrected with Tukey's
481 post-hoc test; mean ± SD). **(F)** (Left) Representative trace of calcium-induced fluorescence in
482 response to AMPA treatment in wild-type and ciRS-7 KO cortical neurons transduced with miR-7 or
483 control lentivirus. (Right) Scatter dot plot of calcium imaging analysis of the cellular response to
484 AMPA in wild-type and ciRS-7 KO cortical neurons infected with control (GFP) or miR-7
485 overexpressing (GFP + miR-7) virus (n = 6-7; **** $p < 0.0001$, Kruskal–Wallis test; central bar
486 represents median value).

487 **DISCUSSION**

488 Here we identify oxygen and glucose deprivation as a metabolic stressor triggering endogenous
489 changes in the ncRNA network of ciRS-7 – miR-7 – Cyrano both *in vitro* and *in vivo* during
490 permanent ischemic stroke. In OGD *in vitro* model, we demonstrate dynamic changes in gene
491 expression for these molecules independent of ciRS-7. In *in vivo* condition of transient ischemic
492 stroke, we found no changes in the lncRNA Cyrano. However, the absence of ciRS-7 reduced cellular
493 death and sensorimotor deficits, while the lack of miR-7 resulted in more extensive tissue damage.
494 This suggests that both ciRS-7 and miR-7 may play a more crucial role in this system. In an *in vitro*
495 model recapitulating the molecular changes occurring during ischemic stroke (low ciRS-7 and high
496 miR-7), these effects were partly executed through miR-7-mediated regulation of glutamatergic
497 signaling, contingent on the absence of ciRS-7. These data suggest that ciRS-7 may regulate miR-7
498 targeting, highlighting an endogenous regulatory role for the ciRS-7/miR-7 network in mediating
499 cellular stress responses under pathophysiological conditions.

500

501 In mice, ciRS-7 harbors 130 binding sites for miR-7[9] and, because of its remarkably high expression
502 in neurons[5,9], the limited molecules of miR-7 in physiological conditions[5] are likely associated to
503 ciRS-7, as indicated by our pyramidal excitatory neurons CLIP-seq data and by others[9,10]. Moreover,
504 Cyrano, highly abundant in neurons, harbors a single nearly complementary site for miR-7 which
505 mediates miR-7 degradation[8]. Our data show that OGD induces changes in the neuronal physiological
506 landscape by concomitant decrease in ciRS-7 and Cyrano and subsequent upregulation of miR-7.
507 These changes seem to be independently regulated, as the absence of ciRS-7 did not influence OGD-
508 induced alterations in the gene expression in miR-7 and Cyrano. While the anticorrelation between
509 Cyrano and miR-7 follow established dynamics, with Cyrano triggering miR-7 degradation through
510 TDMD[8], our study report the induction of miR-7 in the absence of ciRS-7, suggesting that during
511 ischemic stroke the expression of miR-7 does not depend on ciRS-7. Consistently, miR-7

512 overexpression induces ciRS-7 downregulation and this effect is rescued by overexpressing the
513 Cyrano site that mediates miR-7 degradation through TDMD. Moreover, in instances where miR-7
514 suppresses ciRS-7 levels, miR-7 upregulation during OGD becomes even more pronounced.
515
516 The role of miR-7 in ischemic stroke has been studied *in vivo* with controversial results[44,45] and our
517 extensive animal cohort revealed substantial biological variability in the expression levels of miR-7
518 in a mouse model of tMCAo. This outcome is potentially tied to established feedback loops among
519 ciRS-7, Cyrano, and miR-7, as tMCAo in ciRS-7 knockout mice results in a significant
520 overexpression of miR-7 one day post-ischemia, accompanied by a reduced stroke lesion size and
521 motor deficits. Additionally, at 7 dpi, inducible miR-7 knockout mice exhibited an exacerbated
522 ischemic lesion size compared to WT animals, which aligns with literature reporting that miR-7 is
523 necessary for stroke recovery[46] , further suggesting a role for miR-7 in regulating ischemic damage.
524 The transient ciRS-7 KO phenotype is explained by an initial advantage provided by higher miR-7
525 levels, while subsequent ciRS-7 downregulation in WT animals minimizes genotypical differences at
526 later timepoints. Furthermore, our in vitro data, mimicking molecular changes in ischemic conditions
527 (low ciRS-7, high miR-7), indicate that under physiological conditions highly abundant ciRS-7 may
528 function as a buffering system to regulate miR-7 targeting.
529
530 Given the lack of extensive changes in miR-7 targets in both ciRS-7, Cyrano and miR-7 KO animals
531 in physiological conditions[8,9], the exact role of ciRS-7 as an influencer of miR-7 targeting has
532 remained controversial. Our data show a significant shift in the overall expression of miR-7 targets
533 during OGD, where a concerted downregulation of two known miR-7 regulators, ciRS-7 and Cyrano,
534 occurs. Our data suggest that the inducible nature for this network may explain the reported absence
535 of drastic effects on miR-7 targets in physiological conditions. Consistent with this concept, numerous
536 studies show that single miRNA mutants exhibit a phenotype solely under stress conditions[47,48].

537 Moreover, unlike experimental settings involving acute treatment, knock-out models are subjected to
538 the buffering effect of cellular adaptation, as previously experienced[9].
539
540 The analysis of Ago2 CLIP-seq neuronal dataset revealed the lead miR-7 targets downregulated in
541 ciRS-7 KO ischemic mice belong to the functional class of glutamatergic signaling and neuronal
542 outgrowth. Glutamate plays a well-established role in ischemic stroke pathophysiology[12],
543 contributing to neuronal loss through exaggerated release and impaired clearance of glutamate in the
544 synaptic cleft[11]. Intriguingly, ciRS-7 KO neurons exhibit a pronounced sensitivity to glutamate in
545 physiological conditions, which represent a disadvantage in ischemic conditions, due to the
546 susceptibility to glutamate-mediated excitotoxicity. However, ciRS-7 KO neurons do not exhibit
547 increase cellular death upon OGD, but rather present a distinct regulation of processes following
548 OGD response, both *in vitro* and *in vivo*. We propose that the ameliorative effect during ischemic
549 stroke observed ciRS-7 KO mice may be linked to the levels of miR-7 and its unregulated accessibility
550 to targets. In line with this, overexpressing miR-7 dampened the neural glutamatergic response and
551 increased neuronal outgrowth only in ciRS-7 KO neurons, with no effect on the wild-type neurons.
552 A mechanism through which miR-7 partially exerts this role involves targeting the subunit 1 of
553 AMPA receptors (GluR1) by interacting with the 3' UTR of its mRNA, Gria1, thereby dampening
554 the AMPA response. Our data confirms that miR-7 effects on both glutamatergic signaling and neurite
555 outgrowth are dependent on ciRS-7 levels. In line with our results, the effect of miR-7 on neurite
556 outgrowth was previously reported in a neuroblastoma cell line[41] that expresses a negligible amount
557 of ciRS-7 even upon differentiation, suggesting a more direct effect of miR-7 in the absence of its
558 targeting regulator.
559
560 A recent study associates miR-7 with energy homeostasis in hypothalamic neurons[39] during
561 challenging energetic conditions similar to ischemic stroke. However, in this context, alterations in

562 miR-7 were not accompanied by changes in ciRS-7 and Cyrano[39]. Combined with our data revealing
563 diverse dynamics in the activation of the ciRS-7 network by various ischemic insults, this indicates
564 that the network response depends on the type, strength, and duration of the stress and the specific
565 cell type.
566
567 In summary, we propose a regulatory role for ciRS-7-miR-7 in glutamatergic signaling through miR-
568 7 target genes, hence contributing to the control of post-ischemia neuronal damage. Our data support
569 the hypothesis of a role for ciRS-7 in buffering miR-7 effects against unwanted changes, thus
570 behaving as a "safe-guide" system. This study suggests a role of intracellular network of non-coding
571 RNAs in regulating pathophysiological processes in the brain.
572

573 **LIMITATIONS OF THE STUDY**

574 The dynamic nature of multicellular systems, unlike in vitro cultures, results in data incongruencies
575 across different timepoints and stressors. The intrinsic ability of regulatory molecules to induce
576 phenotypic changes even at low doses complicates causality identification in processes involving
577 multiple cellular events, such as disease onset. Growing number of studies revealing non-coding RNA
578 alterations in pathophysiological in vitro systems underscores the necessity for in vivo research to
579 understand the biological relevance of these complex regulatory networks. For a comprehensive
580 analysis of ciRS-7 in ischemic stroke, future studies may benefit from in vivo investigations using
581 Cyrano KO animals and direct rescue experiments on ciRS-7, although these remain technically
582 challenging and time-consuming.
583
584
585

586 # MATERIAL AND METHODS

587 ## PRIMARY AND IMMORTALIZED CELLS

588 ### Primary cortical neuron culture preparation and OGD treatment

589 Primary cortical neurons were prepared from C57BL/6J and C57BL/6N-Cdr1asem1Nikr (Cdr1as KO
590 and their WT counterpart) embryonic day 15 embryonal cortices. After dissection and removal of the
591 meninges, cortices were incubated 15 minutes at 37 °C in a solution of Krebs buffer (0.126 M NaCl,
592 2.5 mM KCl, 25 mM NaHCO3, 1.2 mM NaH2PO4, 1.2 mM MgCl2, 2.5 mM CaCl2, supplemented
593 with 45mM BSA, 0.8% of 3.85% MgSO4 and 1% Pen/Strep, pH 7.4) and 0.025% (w/v) trypsin
594 (Sigma-Aldrich, T 9201). Tissue was then treated with 0.008% w/v DNaseI (Sigma-Aldrich, DN25)
595 and 0.026% w/v trypsin inhibitor (Sigma-Aldrich, T9003) and centrifuged at 300 x g for 3 minutes.
596 Cell pellet was resuspended in 3ml of DNaseI/Trypsin solution and then diluted in 7ml of Krebs.
597 After centrifugation at 300 x g for 3 minutes the pellet containing embryonic neurons was
598 resuspended in cortical neurons growth media: Neurobasal (Gibco 21103049), B27 Supplement
599 (Gibco, 17504044), 0.2 mM L-glutamine (Lonza, BE17-605E), 0.01 mg/ml Penicillin/Streptomycin
600 (Gibco, 15140122). Cells were plated on Poly-D lysine (Sigma-Aldrich, P6407) freshly precoated
601 plates (50 µg/ml in sterile water plates for 1h at 37 °C and washed in sterile water prior use). Different
602 density was used for 6-well plates (1.8 million cells per well), 48-well plates (125.000 cells per well),
603 13mm plastic coverslips (30.000 cells per coverslip). After 5 days in culture half of the in cortical
604 neurons growth media was changed to fresh. Experiments were performed 7 days after the isolation
605 day. Cells were maintained in the incubator 37 °C, 5% CO2. For OGD treatment experiments, before
606 hypoxia induction the media was changed to Normoxic (cortical neurons growth media with
607 Neurobasal changed to Gibco A2477501 supplemented with D-Glucose 25mM and Sodium Pyruvate
608 0.2mM) or OGD (cortical neurons growth media with Neurobasal changed to Gibco A2477501).
609 Normoxic cells were then put back in the incubator, OGD cells were incubated in hypoxic chamber

610 37 °C, 5%CO_2, 1%O_2 (SCI-tive N, Ruskinn Technology). After the OGD timepoint cells were
611 harvested for RNA extraction or subjected to MTT colorimetric test.
612
613 **MTT test**
614 Cell viability was measured from 48-well plates treating the cells with (3-(4, 5-dimethylthiazolyl-2)-
615 2, 5-diphenyltetrazolium bromide), MTT reagent (Sigma-Aldrich, TOX1) diluted with culture media
616 at a final concentration of 120 µM. Triton-X 100 1% v/v (Sigma-Aldrich, X100) treated wells were
617 used as a positive control for this assay. Plates were incubated for 3-5h at +37°C. After, medium was
618 discarded, formazan crystals were dissolved with dimethyl sulfoxide (DMSO) (Sigma-Aldrich,
619 D2650) for 30min at RT in the dark. Absorbance was read at 585nm using Wallac 1420 Victor2
620 microplate reader (Perkin Elmer). Wells without cells were used as background and subtracted from
621 the absorbance data, all the six technical replicates were plotted for each of the three biological
622 replicate and the data was normalized on normoxic WT neurons or WT neurons infected with GFP
623 only.
624
625 **Neurite length measurement**
626 Neurons were seeded at a density of 125.000 cells/well in 48-well plates. After OGD exposure or
627 lentiviral infection, neurons were imaged at day 7 for 48 hours with IncuCyte® S3 Live Cell Analysis
628 System (Essen BioScience Ltd.) in bright field and green channel live cell images (two 10x
629 magnification images per well). Acquired data were analysed with the Incucyte® Neurotrack
630 Analysis Software Module (Sartorius) considering the average value of the two images taken for each
631 of the nine technical replicates for all the three biological replicates.
632
633 **RNA isolation and qRT-PCR**

634 Total RNA was extracted from primary cells and ipsilateral/contralateral animal cortex using
635 TRIzol™ Reagent (Invitrogen) following the manufacturer's instructions. 1µl of GlycoBlue™
636 Coprecipitant (Ambion) was added at the isopropanol step in each sample. RNA was quantified using
637 a Nanodrop 2000 spectrophotometer. 1 µg of total RNA was used for reverse-transcription of
638 mRNAs, circRNA, lncRNAs and pri-miRNA species with High-Capacity cDNA Reverse
639 Transcription Kit (Applied Biosystems) following the manufacturer's protocol. SYBR Green qPCR
640 Master Mix (High ROX) (Bimake) and custom designed oligos were used to quantify mRNAs,
641 circRNAs, and lncRNAs following the manufacturer's indications. Mature microRNAs were reverse-
642 transcribed with TaqMan™ MicroRNA Reverse Transcription Kit (Invitrogen) using miRNA-
643 specific primers supplied in the TaqMan® probe kit for qPCR following the manufacturer's protocol.
644 Mature microRNAs and pri-microRNA PCRs were performed using Maxima Probe/ROX qPCR
645 Master Mix (Invitrogen) and TaqMan® specific probes (Thermofisher) following the manufacturer's
646 protocol. The result was analyzed with the ΔΔCT method and normalized geometric mean of 2
647 internal normalization controls (Gapdh and Rplp0) for SYBR green qPCRs and U6 expression for
648 TaqMan® miRNA and pri-miRNA. TaqMan® probes and sequence of the SYBR Green
649 oligonucleotide primers is available in the Supplementary Table S9.
650

651 **Lentivirus vectors and virus generation**

652 Lentiviral vectors LV1-eGFP (control) or LV1-eGFP-miR-7 were generated by subcloning inserts
653 from pAAV_hSYN1-eGFP-miR-7 and pAAV_hSYN1-eGFP (provided by Thomas B. Hansen)
654 inside LV1 (immunodeficiency virus 1 (HIV-1)-based LV-PGK-GFP) backbone by GenScript
655 Biotech Corporation. The generated construct contained HIV-1-LV backbone with hSYN1-eGFP-
656 miR-7 insert instead of PGK-GFPN inserted creating a terminal SmaI (CCCGGG) and a C-terminal
657 ApaI (GGGCCC) flanking restriction sites. The same was performed for the control vector with
658 hSYN1-eGFP insert only. In addition, GenScript Biotech Corporation generated lentiviral vectors,

659 namely LV1-mCherry-CR1 and LV1-mCherry-MUT, for the overexpression of the Cyrano CR1
660 region involved in miR-7 degradation through TDMD or a mutated form of it. The sequences for
661 these inserts were obtained from the prior publication by Kleaveland et al (2018)[8] and are accessible
662 on Addgene (https://www.addgene.org/128768/, https://www.addgene.org/128748/). These
663 sequences were then cloned into the previously established LV1-hSYN backbone, with the creation
664 of terminal AgeI (ACCGGT) and C-terminal SalI (GTCGAC) sites.
665 3rd generation lentiviral particles were produced by the BioCenter Kuopio National Virus Vector
666 Laboratory in Kuopio, Finland. The viral titer was assessed through qPCR serial dilution
667 quantification using eGFP or mCherry ReadyMade™ Primers (IDT) (Supplementary Table S9).
668 Work with the virus vectors was carried out under permission from Finnish National Supervisory
669 Authority for Welfare and Health, Valvira. Cells were infected at day 2 post isolation with MOI 0.5
670 achieving 80% positive infected cells assessed by GFP or mCherry expression in fluorescent
671 microscope (Supplementary Figure 7A,D) at day 7. The amount of overexpression of miR-7 or
672 Cyrano CR1 region was assessed by qPCR as above specified (Supplementary Figure 7B,E).
673
674 **Library preparation OGD cortical neurons**
675 All the samples RNA were isolated with TRIzol™ Reagent (Invitrogen) as specified above. RNA
676 samples were treated with TURBO DNA-free™ Kit (Ambion) following the manufacture's
677 instruction. RNA integrity was assessed through Agilent Bioanalyzer 2100 system with the Agilent
678 RNA 6000 Nano. The concentration of the samples was established with Qubit™ RNA Extended
679 range kit (Invitrogen). From cortical neurons subjected to OGD we generated 1) library to detect
680 circularRNAs and mRNA and lncRNAs using SMARTer® Stranded Total RNA Sample Prep Kit
681 (Takara Bio USA, Inc.) and 2) library for miRNAs detection utilizing NEBNext® Small RNA Library
682 Prep Set for Illumina (New England Biolabs (UK) Ltd) quality checked and size selected using pippin
683 prep method following manufacturer's protocol. All the libraries were generated following the

684 manufacturer's protocol. After generation, the libraries were quantified with Qubit™ High Sensitivity
685 DNA kit (Invitrogen) and by qPCR using KAPA Library Quantification Kit for Illumina® Platforms
686 (Roche). Library size was determined with Agilent Bioanalyzer 2100 system using the Agilent High
687 Sensitivity DNA Kit. Cortical neurons samples to detect circularRNAs, mRNA, and lncRNAs were
688 sequenced paired-end 100 cycles on NovaSeq™ 6000 platform (Illumina) and single-read 75 cycles
689 on NextSeq™ 500 system (Illumina) to detect microRNAs.
690
691 **Calcium imaging**
692 Calcium imaging was performed with murine E15 cortical neurons. The neurons were plated onto
693 PDL-coated circular plastic coverslips (13 mm diameter) in 12-well plate at a density of 30,000
694 cells/coverslip and kept for 5 days in Neurobasal medium supplemented with B27. To quantify and
695 compare the functional expression of glutamate and GABA receptors in neuronal cultures, we used
696 calcium-imaging technique as previously described[49]. Briefly, neuronal cultures were loaded with the
697 cell-permeable indicator Fluo-4am (Life Technologies, F10471) for 30 min at 37 °C, followed by 10
698 min washout, and placed in the perfusion chamber mounted on the stage of Olympus IX7010
699 microscope. Neurons were continuously perfused by basic salt solution (BSS) 3 ml/min containing
700 in mM: 152 NaCl, 10 HEPES, 10 glucose, 2.5 KCl, 2 CaCl2, 1 MgCl2 and pH adjusted to 7.4. Test
701 compounds diluted in the BSS to final concentrations were applied through fast perfusion system
702 (Rapid Solution Changer RSC-200, BioLogic Science Instruments). Cells were imaged with 10x
703 objective using Olympus IX-7010. Excitation wavelength was set as 494 nm, sampling frequency 2
704 FPS. Glutamate (100 µM with the co-agonist glycine 10 µM promoting activation of NMDA
705 receptors subtype) or GABA (100 µM) were applied for 2 s. Finally, KCl (50 mM) application for 2 s
706 was used to distinguish excitable neurons from possible non-neuronal cells. Fluorescence was
707 detected with the Till Photonics imaging system (FEI GmbH) equipped with a 12-bit CCD Camera
708 (SensiCam) with a light excitation wavelength of 494 nm. Calcium responses to neurotransmitters

709 were evaluated from changes in fluorescence intensity of individual neurons. To this end, regions of
710 interest (ROI) of round shape around the cell body were selected from the whole image with the TILL
711 vision Imaging Software (TILL Photonics GmbH). To distinguish from non-neuronal cells, ROI was
712 taken at the time point corresponding to KCl-induced activation of neurons. The intensity values in
713 each ROI were averaged at each time point to form a fluorescence signal for each neuron and
714 normalized to the baseline level. Signals above 5% of the baseline were included in the analysis.
715
716 **N2a Cell culture**
717 Immortalized murine neuroblastoma cells (N2a) were maintained in DMEM, high glucose,
718 GlutaMAX™ Supplement (Gibco, 31966021) media supplemented with supplemented with 10%
719 Fetal Bovine Serum (Gibco, 10270106) and 1% penicillin and streptomycin in temperature controlled
720 humidified incubator (37 °C, 5%CO_2). As previously published[50], for differentiation induction
721 100.000 cells were plated in a 6-well plate and maintained in complete media supplemented with
722 20µM retinoic acid (Sigma-Aldrich, R2625) in dimethyl sulfoxide (DMSO) with or without serum
723 starvation (2% FBS instead of 10%) changing half of the media every second day for 5 days before
724 collection.
725
726 **Luciferase assay**
727 Human embryonic kidney 293 cells containing the SV40 T-antigen (HEK293T) were cultured in
728 DMEM, high glucose, GlutaMAX™ Supplement (Gibco, 31966021) medium, supplemented with
729 10% Fetal Bovine Serum (Gibco, 10270106), and 1% penicillin and streptomycin in a temperature-
730 controlled humidified incubator (37 °C, 5%CO2). For the luciferase assay, 20,000 cells were seeded
731 per well in a 96-well plate. The following day, cells were co-transfected with 100ng of murine Gria1
732 3' UTR renilla/luciferase plasmid (MmiT076857-MT06-GC, GeneCopoeia) or miRNA 3' UTR target
733 control plasmid (CmiT000001-MT06-GC, GeneCopoeia) and 100nM of either miRIDIAN miRNA

734 mimic of mmu-miR-532 (C-310769-01-0002, Dharmacon) as a negative control or mmu-miR-7a-5p
735 (C-310591-07-0002, Dharmacon) using Lipofectamine™ 2000 (11668030, Invitrogen) according to
736 the manufacturer's protocol. After 48 hours, the luciferase assay was conducted with the Luc-Pair
737 Luciferase Assay Kit 2.0 (LF001-GC, GeneCopoeia), following the manufacturer's instructions,
738 except for the cell lysis step, which was performed directly on the plate in lysis buffer using three
739 freeze and thaw cycles with dry ice. Luciferase data were normalized to Renilla expression and
740 presented as the Fold Change of Relative Fluorescence between the samples with respect to 3' UTR
741 vector overexpression alone.

742 **MOUSE STRAINS AND ANIMAL PROCEDURES**

743 All experiments follow the Helsinki Declaration and guidelines set by the European Commission
744 (European Communities Council Directive, 86/609/EEC) and were approved by the National Animal
745 Experiment Board of Finland. Animals were housed with same sex siblings, in controlled
746 temperature, humidity and light (12 hours light/dark cycle) conditions. Animals had access to ad
747 libitum food. Before the beginning of the animal study mice were divided in single cages. Mice were
748 randomized and all the participants were blinded to the genotype (surgery, MRI acquisition,
749 behavioral test, sample collection and data analysis). Prior to the surgery, we use random number
750 generator (GraphPad Prism quick calcs https://www.graphpad.com/quickcalcs/randomN1/) to
751 randomize the mice into treatment groups. This numbering has been used in crescent order on 3-4
752 months old male mice that were divided into groups. pMCAO study was performed on 3-4 months
753 old BALB/cOlaHsd male mice (n = 6-8 per timepoint). Cdr1as (ciRS-7) KO tMCAO study was
754 performed on 3-4 months old C57BL/6N-Cdr1asem1Nikr[9] (Cdr1as KO mice and the WT
755 counterpart), provided by Prof. Dr. Nikolaus Rajewsky, MDC, Berlin, Germany (n = 22-24 per
756 genotype). miR-7 inducible KO tMCAO study was performed on 3-4 months old B6.Cg-
757 miR7a1tm1(fl/fl)ms miR7a2tm1(fl/fl)ms miR7btm1(fl/fl)ms Ndor1Tg(UBC-cre/ERT2)1Ejb/Stf and

758 UBC-cre negative counterpart[39] provided by Prof. Dr. Markus Stoffel, ETH, Zurich, Switzerland (n
759 = 20-26 per genotype).

760 **Genotyping**

761 Before the animal studies, ciRS-7 KO and miR-7 KO mice were genotyped as before[9,39] except for
762 the tissue dissociation step. Briefly, ear puncture samples were digested in 50 mM Sodium Hydroxide
763 solution for one hour at 95 °C. Once equilibrated to room temperature the samples were neutralized
764 with 1M Tris Hydrochloride pH 8. Two microliters of digested samples were used to run the reaction
765 of PCR with Taq 2X Master Mix (New England Biolabs (UK) Ltd) following manufacturer protocol
766 and using the oligonucleotide primers as specified in Supplementary Table S9. The PCR products
767 were separated on a stained 2.5% or 1.5% Agarose gel for ciRS-7 and miR-7 KO respectively and
768 run in an electrophoresis chamber. Images were acquired with ChemiDoc Imaging Systems (Bio-Rad
769 Laboratories, Inc).

770

771 **Permanent middle cerebral artery surgery (pMCAo)**

772 Permanent middle cerebral artery occlusion (pMCAo) was performed in 3-4 months old
773 BALB/cOlaHsd male mice as previously described[51]. Briefly, mice were anesthetized using 5%
774 isoflurane and anesthesia was maintained with 2% isoflurane. Temperature of the animals was
775 controlled during the surgery with heating blanket and rectal probe (Harvard apparatus). After the
776 skin incision, the left temporal bone was exposed under the temporal muscle, and 1 mm hole was
777 drilled on top of bifurcation in the middle cerebral artery (MCA). The dura was gently removed, and
778 the MCA was lifted and permanently occluded under the bifurcation using a thermocoagulator (Aaron
779 Medical Industries Inc.). Success of the occlusion was confirmed by cutting the MCA above the
780 occlusion site. After the occlusion, the temporal muscle was replaced, and the wound was sutured.
781 The surgery was performed on a total of 20 mice, 3 mice (one per timepoint) died during the surgery
782 and was then not included.

783

784 **miR-7 KO induction with tamoxifen**

785 Before tMCAO surgery, miR-7 inducible KO mice were injected with 2mg of Tamoxifen
786 intraperitoneally once per day for 5 consecutive days at the age of 3 to 4 weeks as before[39].
787 Recombination was induced in both Cre+ and Cre- littermates. Tamoxifen (Sigma-Aldrich, T5648)
788 was resuspended in 90% corn oil (Sigma-Aldrich, C8267) and 10% pure ethanol and dissolved at
789 56°C for 30 minutes in the dark. After injection the mice were put on soft food diet and their weight
790 was monitored daily. Mice showing a successful genomic recombination in ear puncture samples two
791 weeks after injection were included in the study (Supplementary Figure S5A). At the end of the study
792 the animals were analyzed for miR-7 abrogation in the brain through RT-qPCR (Supplementary
793 Figure S5B).

794

795 **Transient middle cerebral artery surgery (tMCAO)**

796 Transient middle cerebral artery occlusion (tMCAO) was chosen to continue the in vivo stroke studies
797 as pMCAO in C57BL/6J produces considerably smaller infarcted regions than in the BALB/c
798 background[52,53]. For this reason tMCAO was performed in 3-4 months old male Cdr1as and miR-7
799 KO and WT mice as previously described[54]. Briefly, induction of anesthesia was performed with 3.5-
800 4% isoflurane in 0.5 L/min of 100% O2-enriched air and maintained at 1-1.5% isoflurane during the
801 surgery. The body temperature maintained at 36 ± 1°C during surgery with a heating pad attached to
802 a rectal probe. A Doppler probe was fixed on the temporal bone over the MCA to monitor blood flow.
803 The right common, external, and internal carotid arteries (CCA, ECA, and ICA) were exposed
804 through an incision in the neck. The arteries were carefully dissected, and a 6-0 silicon coated
805 monofilament of 0.21 mm of diameter (Doccol Corporation) was inserted into the right CCA or left
806 ECA (Cdr1as and mir-7 KO respectively) and led through the ICA until blocking the origin of the
807 MCA. Blood flow blockage was monitored with the Doppler probe, and animals with less than 80%

808 of blood flow decrease were discarded. After one hour of occlusion, the monofilament was withdrawn
809 allowing blood reperfusion. Animals that did not show a correct reperfusion measured by laser
810 doppler were discarded from the study. Incisions were permanently sutured, and the animals were
811 allowed to recover in a temperature-controlled environment for 24 hours. The surgery was performed
812 on a total of 32 WT and 25 Cdr1as KO mice, and 36 WT and 26 miR-7 KO. In the ciRS-7 animal
813 study a total of 7 mice was excluded as: 2 KO and 2 WT mice lacked reperfusion upon surgery, 2
814 WT and 1 KO mice died during the study. In the miR-7 animal study a total of 12 mice was excluded
815 as: 3 WT and 2 KO lacked reperfusion upon surgery, 4 WT and 3 KO died during the study.
816
817 **Magnetic resonance imaging (MRI)**
818 MRI was performed at 1, 3, and 7dpi using a vertical 9.4 T/89 mm magnet (Oxford instrument PLC)
819 upon anesthesia with 1.8% isoflurane in 30% O2/70% N2O. We acquired twelve slices of 0.8mm
820 thickness per mouse (echo time 40ms, repetition time of 3000ms, matrix size of 128 × 256 and field
821 of view 19.2 × 19.2 mm^2) and analyzed the first seven images using the Aedes software
822 (http://aedes.uef.fi/) for MatLab program (Math-works). Upon definition of the region of interest
823 (ROI) of contralateral, ipsilateral, and lesion, the lesion volume normalized on oedema was calculated
824 on the first 7 section as: $Corrected\ lesion\ size = lesion\ size \times \Big(1 -$
825 $\frac{[ipsilateral\ size - contralateral\ size]}{contralateral\ size}\Big)$. The lesion size is expressed has percentage of lesion on the total
826 brain size.
827
828 **Neurological severity score (NSS)**
829 Mice were examined for neurological deficits at baseline and dpi 1, 3, and 7 using a severity scale
830 comprising the following tests: postural reflex, circling, falling to contralateral side, placement of the
831 contralateral forelimb during motion, and general state of alertness or consciousness. Deficits were

832 graded from 0 (normal) to 2 or 3 (severe)[55]. A sum of these scores were used for statistics. Behavioral
833 assessment was performed by an experimenter blinded to the genotype of mice.
834
835 **Transcardiac perfusion and sample collection**
836 After anesthesia, mice were perfused transcardially with cold saline solution with heparin 2500 IU/l
837 (Leo Pharma A/S). In the pMCAo study, the brains were collected and dissected into contralateral
838 and peri-ischemic cortical regions. In the tMCAO study the brains were cut in 6 coronal sections and
839 stained with 1% 2,3,5-Triphenyltetrazolium Chloride (TTC) (Sigma-Aldrich) in PBS solution for 5
840 minutes at 37 °C in agitation before dissection of contralateral and peri-ischemic cortical regions. For
841 immunohistochemistry staining, brains were collected and fixed in 4% paraformaldehyde solution in
842 0.1 M phosphate buffer (PB) pH 7.4. After 22 hours of fixation, the brains were transferred in 30%
843 sucrose in PB buffer solution for 48 hours and then frozen in liquid nitrogen before being stored in -
844 70 °C.
845
846 **GFAP immunostaining**
847 Each brain was then cut using a cryostat (Leica Microsystems) into six 20 µm coronal sections 400 µm
848 apart, collected on Superfrost™ Plus Microscope Slides (ThermoFisher Scientific) and stored in -
849 70°C until immunostaining. Sections were then rehydrated with phosphate-buffered saline (PBS) pH
850 7.4 for 10 min and PBS with 0.05% Tween-20 (PBST) (Sigma-Aldrich) for 5 min. Endogenous
851 peroxidase was blocked by using 0.3 % hydrogen peroxide (H_20_2) in MeOH for 30 min after which
852 sections were washed 3 x 5 min in PBST. Non-specific binding was blocked with 10 % normal goat
853 serum (NGS)(Vector, S-1000) in PBST for 1 h at RT Sections were incubated overnight at RT in
854 primary antibody rabbit anti-GFAP (Agilent, Dako Z0334,1:500 in 5 % NGS-PBST) and then with
855 biotinylated secondary antibody anti-rabbit IgG (H+L) (Vector, BA-1000, 1:200 in 5 % NGS-PBST)
856 for 2 h at RT followed by incubation in ABC reagent (Vector Elite Kit) for 2 h at RT. Sections were

857 washed 3 x 5 min in PBST before and after the incubations. Nickel-3,3'-diaminobenzidine (Ni-DAB)
858 solution (0.175M Sodium acetate, 1% Nickel ammonium sulphate, 50mg DAB (Sigma-Aldrich, D-
859 5905)) with 0.075 % H_20_2 was used to develop the colour for 6 min stopping the reaction by washing
860 the sections 2 x 5 min in dH_2O. Sections were then dehydrated in 50 % EtOH, 70 % EtOH, 95 %
861 EtOH, 100 % EtOH for 2 min in each and 3 x 5 min in xylene followed by mounting the coverslips
862 with Depex.
863
864 **Image acquisition & analysis**
865 Six GFAP immunoreactivity light microscope images per mouse were acquired by Leica DM6B-Z
866 Thunder Imager microscope (Leica Microsystems CMS GmbH) equipped with DMC2900 camera
867 using 10x magnification. Images were captured using LAS X software (Leica Microsystems CMS
868 GmbH) with exposure time 5 ms, color-gain mode: R:0-G:0-B:25. The images were quantified from
869 the peri-ischemic cortex next to the lesion border (1mm) and the corresponding area of the healthy
870 contralateral hemisphere from 10x images using ImageJ software[56] function "Measure particles". The
871 results were presented as relative immunoreactive area to the total area analyzed. This part of the
872 work was carried out with the support of UEF Cell and Tissue Imaging Unit, University of Eastern
873 Finland, Biocenter Kuopio and Biocenter Finland.
874
875 **Library preparation tMCAO tissue samples**
876 All the samples RNA were isolated with TRIzol™ Reagent (Invitrogen) as specified above. RNA
877 samples were treated with TURBO DNA-free™ Kit (Ambion) following the manufacture's
878 instruction. RNA integrity was assessed through Agilent Bioanalyzer 2100 system with the Agilent
879 RNA 6000 Nano. The concentration of the samples was established with Qubit™ RNA Extended
880 range kit (Invitrogen). We generated a library from ciRS-7 WT and KO tMCAO animals contralateral
881 and peri-ischemic cortices to detect mRNAs changes using CORALL total RNA-Seq Library Prep

882 Kit (Lexogen GmbH) after ribosomal RNA depletion of 600ng of RNA with RiboCop rRNA
883 Depletion Kit V1.2 (Lexogen GmbH). All the libraries were generated following the manufacturer's
884 protocol. After generation, the libraries were quantified with Qubit™ High Sensitivity DNA kit
885 (Invitrogen) and by qPCR using KAPA Library Quantification Kit for Illumina® Platforms (Roche).
886 Library size was determined with Agilent Bioanalyzer 2100 system using the Agilent High Sensitivity
887 DNA Kit. Animal samples were sequenced single-read 75 cycles on NextSeq™ 550.

888 **DATA ANALYSIS**

889 **RNA-seq data analysis**

890 Bulk RNA sequences of mRNA and miRNA have been aligned and quantified to the mouse genome
891 of reference mm10 with the Cdr1as annotation of "chrX:61183248|61186174|.|+" using the and 1.1.0
892 version of "smrnaseq" applied without clipping and the three prime adapter
893 "AGATCGGAAGAGCACACGTCT"), while circular sequences using 1.1 CIRIquant[57] set to Read
894 1 matching the sense strand. Count data were prepared following the workflow defined by Law et
895 al[58]. We filtered out lowly expressed molecules in any condition using the function "filterByExpr" to
896 increase the reliability of the mean-variance relationship. We removed the differences between
897 samples due to the sequencing depth normalizing the count using the trimmed mean of M-values
898 (TMM)[59] method and applied a log transformation minimizing sum of sample-specific squared
899 difference to enhance the true positive and negative ratio in the downstream analysis[60]. We checked
900 for batch effect due to different timings in biological replicates preparation by performing a principal
901 component analysis and unsupervised consensus clustering with Cola[61]. We identified a batch effect
902 due to different timings in biological replicates preparation influencing the grouping of the normoxic
903 and OGD samples in the dataset ciRS-7 KO/WT cortical neurons (Supplementary Table S5). We
904 corrected the batch effect of this dataset using the negative binomial regression from Combat[62]. We
905 adjusted the variance between the samples as before[63] through winsorization[64]. We finally created
906 the design matrix for each pair of conditions to compare (contrast) and performed the differential

907 expression analysis using limma/edgeR model[58] controlling for the false discovery rate with
908 Benjamini-Hochberg Procedure[65]. We employed an interaction term in differential expression
909 analysis to assess whether the OGD response varied between ciRS-7 KO and WT backgrounds. Our
910 analysis using the interaction term identified only one significant DE gene, Gm2004, with a logFC
911 change of 9.631571, aligning with our expectations (Supplementary Table S6). This outcome
912 emphasized that the lack of ciRS-7 did not modulate the OGD response per se and that our
913 backgrounds remained consistent.
914
915 **Ingenuity Pathway Analysis (IPA) and Functional enrichment analysis**
916 We uploaded the differentially expressed genes of each contrast to QIAGEN IPA (QIAGEN Inc.,
917 https://digitalinsights.qiagen.com/IPA)[66] and Metascape[67] for Ingenuity pathway analysis and
918 functional enrichment analysis, respectively. The analysis has been performed with default
919 parameters and IPA's background was composed of non-differentially expressed genes.
920
921 **Deconvolution analysis with scRNAseq**
922 Deconvolution aims to estimate the proportions of different cell types within a mixed population in
923 bulk RNA sequencing data using expression profiles from individual cells of scRNA-seq data and
924 represents them in a composite expression profile. The term "contribution" is used to describe the
925 proportion of gene expression attributed to a specific cell type, such as astrocytes or neurons, within
926 the composite profile. We exploited cell-type specific gene expression from external single-cell RNA
927 sequencing (scRNA-seq) data to define the cell subpopulations composing our cortical neuron culture
928 (Supplementary Table S2) and ischemic stroke animal tissue (Supplementary Table S7) bulk RNA
929 sequencing datasets. The scRNA-seq dataset of Loo et al.[68] of the mouse cerebral cortex at embryonic
930 day 14.5 was provided to SCDC[69] for performing the deconvolution of our gene expression matrix
931 with cortical neuron samples in normoxic conditions. The scRNA-seq data of Zeisel at al.[70] composed

932 of murine cerebral cortex samples from p25 to p60 was instead provided to MuSiC[71] to perform the
933 deconvolution of our gene expression matrix with contralateral and peri-ischemic samples of wild-
934 type and ciRS-7 KO ischemic stroke animals (Supplementary Table S7) as this method is designed
935 to work with multi-subject scRNA-seq dataset.
936
937 **GRO-seq data analysis**
938 A summary of all GRO-seq samples used to quantify pri-miRNA expression levels are presented in
939 Supplementary Table S3. Raw reads for public GRO-seq data were acquired from the GEO database.
940 GRO-Seq reads were trimmed using the HOMER v4.3 (http://homer.salk.edu/homer)[72] software to
941 remove A-stretches originating from the library preparation. From the resulting sequences, those
942 shorter than 25 bp were discarded. The quality of raw sequencing reads was controlled using the
943 FastQC tool (http://www.bioinformatics.babraham.ac.uk/projects/fastqc)[73] and bases with poor
944 quality scores were trimmed using the FastX toolkit (http://hannonlab.cshl.edu/fastx_toolkit/). Reads
945 were aligned to mouse mm9 reference genome using the Bowtie[74] version bowtie-0.12.7. Up to two
946 mismatches and up to three locations were accepted per read and the best alignment was reported.
947 The data was used to create Tag Directories using HOMER. To optimize coverage, a combined tag
948 directory representing all samples of a given cell type (under one or several GSE numbers) was
949 created and used for pri-miRNA quantification using the 'analyzeRepeats.pl' command and '-rpkm -
950 strand +' options".
951
952 **miRWalk analysis**
953 We associated the significantly deregulated miRNAs and differentially expressed genes of wild-type
954 and ciRS-7 KO cortical neurons subjected to OGD (Supplementary Table S2, Supplementary Table
955 S5). We filtered miRNA-Target interactions obtained from 3.0 miRWalk[75,76] database with 99%
956 probability and located in the 3' UTR region and included Oip5os1 (Cyrano) as target of mmu-miR-

957 7a-5p[8]. We linked the differentially expressed miRNAs and genes of each contrast by anticorrelation
958 (e.g. miRNA with positive log fold change and significant adjusted probability value is associated to
959 genes with negative log fold change, significant adjusted probability value and targets in miRWalk
960 of the miRNA) focusing on mmu-miR-7a-5p.
961
962 **CDF generation**
963 We tested the assumption of anticorrelation between mmu-miR-7a-5p and its miRWalk gene targets
964 using the empirical Cumulative Distribution Function (eCDF). For each contrast, we compared the
965 eCDF (control function) obtained from the values of log fold change of the non-target genes against
966 the one of the miRNA's targets and tested their equality with the Kolmogorov–Smirnov test[77]. Genes
967 characterized by longer 3' UTRs often possess a greater number of potential miRNA binding sites
968 and may display distinct expression characteristics owing to their intrinsically less stable nature. To
969 address this concern, we have incorporated a normalization approach inspired by Kleaveland *et al.*
970 (2018)[8] in which the relationship between fold change and 3' UTR length is fitted to a linear function
971 using the 3' UTR length annotated by Eichhorn *et al.* (2014)[78]. The original fold changes are adjusted
972 by subtracting predicted values, assuming these values exclusively represent expected fold changes
973 due to 3' UTR length. This subtraction is done as absolute values to adjust the magnitude of the
974 original fold change, based on the assumption that 3' UTR length, as a gene-specific attribute, is
975 independent of class order. The subtraction aims to eliminate the fold change component attributed
976 to 3' UTR length and retain the component associated with miRNA targeting. To determine the
977 magnitude and direction of the shift of the eCDF of the targets in respect of the non-targets, we
978 measured the area between the two curves following this formula: $\int \{F_Y(t) - F_X(t)\}\, dt$ and the
979 Wasserstein distance[79]. Both the considered targets and non-targets genes passed the filtering by
980 expression, count normalization and participated at the differential expression analysis.
981

982 **CLIP-seq analysis**

983 We collected the HITS-CLIP dataset of Argonaute 2 in pyramidal excitatory neurons produced by
984 Tan et al.[40] (GSE211552) and replicated the original analysis to map and annotate the genomic
985 regions with a significant read cluster (peak) (Supplementary Table S8). Briefly, we performed a
986 quality control with FastQC (http://www.bioinformatics.babraham.ac.uk/projects/fastqc)[73] and
987 applied trimming to remove bases after 50 base pairs due to low quality. We applied Cutadapt[80] to
988 remove adapters and over-represented sequences. We selected reads of at least 24 nucleotides in
989 length and quality score higher than 20 for each nucleotide. Reads were aligned to the mouse
990 reference genome mm10 using Burrows-Wheeler aligner[81] with default parameters, then the mapped
991 reads were expanded by 30 nucleotides on each side. We considered only reads present in at least 2
992 experimental replicates and clusters composed of at least 10 overlapping reads. Bowtie[82] was used to
993 map all occurrences of sequences complementary to the 6mer seed sequence (positions 2-7 of the
994 mature miRNA) of mouse miRNAs from miRBase V21 (https://www.mirbase.org/) to the mouse
995 genome mm10, allowing no mismatches. Strand specific intersection was done with the filtered
996 clusters in the 3' UTR, 5' UTR, coding sequence (CDS) and intron regions from RefSeq gene
997 definitions, as well as antisense matches to RefSeq genes[83]. Strand specific intersection was also done
998 to circRNAs from circBase[84]. This generated a genome-wide list with predicted miRNA target sites
999 backed by the detected Ago2 HITS-CLIP clusters for all mouse miRNAs. A subset including all miR-
1000 7a-5p targets is supplied as Supplementary Table S8. Only 3' UTR target sites were used to define
1001 miRNA mediated regulation. The full list of all predicted miRNA target sites was uploaded to GEO,
1002 as described in the Data Availability section. We conducted quality control on the CLIP-seq output
1003 by using MEME-ChIP[85] (https://meme-suite.org/meme/tools/meme-chip), a dedicated tool for motif
1004 enrichment analysis. This tool allowed us to systematically explore the enrichment of miRNA binding
1005 motifs within all identified CLIP-seq 3' UTR clusters. The results of this analysis are provided in
1006 Supplementary Table S8.

1007

1008 **Statistical analysis**

1009 Graphs and statistical analysis were performed in GraphPad Prism 9. Every Figure legend reports
1010 parameters of replicates (n), statistical test and p-value obtained. Where not specified, p-value was
1011 not statistically significant (p-value > 0.05). We refer to n in animal study as single biological
1012 replicate (mouse) and in cortical neuron as technical replicates in the same batch, the experiment has
1013 been performed in three independent biological replicates.

1014

1015 **Data availability**

1016 The data produced and analyzed in this publication have been deposited in NCBI's Gene Expression
1017 Omnibus[86] and are accessible through GEO Series accession number GSE213179, GSE213067,
1018 GSE213177, GSE211552 and GSE215210. The code developed to analyze the data produced in this
1019 study is deposited in Zenodo at https://zenodo.org/records/10489728.

1020 ACKNOWLEDGEMENTS

1021 We thank Nicholas Downes, Mirka Tikkanen, Reetta Vuolteenaho, Miia Salo, Irina Belaia, Nikita
1022 Mikhailov, and Gianluca Como for their support. We acknowledge UEF Biocenter Kuopio In Vitro
1023 and Ex Vivo Electrophysiology Core Facility, National Virus Vector Laboratory Service, Cell and
1024 Tissue Imaging Unit, Lab Animal Centre (Nina Liimatainen and Hanna Miettinen), Biocenter Oulu
1025 Transgenic and Tissue Phenotyping Core, Oulu Laboratory Animal Centre Research Infrastructure,
1026 Translational Cell Biology Core at Kontinkangas Campus, and the Faculty of Biochemistry and
1027 Molecular Medicine of the University of Oulu. This project received co-funding from the Horizon
1028 2020 Framework Programme of the European Union (Marie Skłodowska Curie grant agreement No
1029 740264), as well as the Academy of Finland, Finnish Cultural Foundation, Finnish Foundation for
1030 Cardiovascular Research, Instrumentarium Science Foundation, Inkeri and Mauri Vänskä

1031 Foundation, Saastamoinen Foundation, Kuopio University Foundation, Aarne and Aili Turusen
1032 Foundation, and Aarne Koskelo Foundation. Illustrations were created with BioRender.com.

1033 AUTHOR CONTRIBUTIONS

1034 F.S. and T.M. conceived and planned the study, with intellectual contributions from T.H., J.J., R.
1035 Giniatullin, and D.T. In vivo experiments involved F.S., V.S., P.K., I.U., J.J., H.D., C.P., N.V, and J.
1036 Koistinaho. In vitro experiments involved F.S., V.S., D.M.T., M.G.B., R. Giniatullina, N.K., E.G.,
1037 S.YH. RNA-seq experiments involved F.S., A.H.S., J.S., and J. Kjems, with analysis performed by
1038 L.G. Transgenic animals and study assistance were provided by M.L., M.P., M.S., N.R. HITS-CLIP-
1039 seq was generated and analyzed by M.V. and A.S. GRO-seq was analyzed by M.K. Sample
1040 preparation at Oulu University was done by R.H., F.S., V.S., S.K., and A.H. F.S. and T.M., wrote the
1041 manuscript with input from T.H., J.J., R. Giniatullin, J. Kjems, and critical feedback from all authors.

1042 CONFLICT OF INTEREST

1043 The authors declare no competing interests.

1044 REFERENCES

1045

1046 1. Mehler, M. F. & Mattick, J. S. Noncoding RNAs and RNA editing in brain development,
1047 functional diversification, and neurological disease. *Physiol Rev* **87**, 799–823 (2007).
1048 2. Lewis, B. P., Burge, C. B. & Bartel, D. P. Conserved seed pairing, often flanked by adenosines,
1049 indicates that thousands of human genes are microRNA targets. *Cell* **120**, 15–20 (2005).
1050 3. Mattick, J. S. & Makunin, I. V. Small regulatory RNAs in mammals. *Hum Mol Genet* **14 Spec**
1051 **No 1**, R121-132 (2005).

1052 4. Fatica, A. & Bozzoni, I. Long non-coding RNAs: new players in cell differentiation and
1053 development. *Nat Rev Genet* **15**, 7–21 (2014).
1054 5. Hansen, T. B. *et al.* Natural RNA circles function as efficient microRNA sponges. *Nature* **495**,
1055 384–388 (2013).
1056 6. Kristensen, L. S. *et al.* The biogenesis, biology and characterization of circular RNAs. *Nat Rev*
1057 *Genet* **20**, 675–691 (2019).
1058 7. Hansen, T. B. *et al.* miRNA-dependent gene silencing involving Ago2-mediated cleavage of a
1059 circular antisense RNA: miRNA mediated cleavage of circular antisense RNA. *The EMBO*
1060 *Journal* **30**, 4414–4422 (2011).
1061 8. Kleaveland, B., Shi, C. Y., Stefano, J. & Bartel, D. P. A Network of Noncoding Regulatory
1062 RNAs Acts in the Mammalian Brain. *Cell* **174**, 350-362.e17 (2018).
1063 9. Piwecka, M. *et al.* Loss of a mammalian circular RNA locus causes miRNA deregulation and
1064 affects brain function. *Science* **357**, eaam8526 (2017).
1065 10. Memczak, S. *et al.* Circular RNAs are a large class of animal RNAs with regulatory potency.
1066 *Nature* **495**, 333–338 (2013).
1067 11. Olney, J. W., Rhee, V. & Ho, O. L. Kainic acid: a powerful neurotoxic analogue of glutamate.
1068 *Brain Res* **77**, 507–512 (1974).
1069 12. Dirnagl, U., Iadecola, C. & Moskowitz, M. A. Pathobiology of ischaemic stroke: an integrated
1070 view. *Trends Neurosci* **22**, 391–397 (1999).
1071 13. Tiedt, S. & Dichgans, M. Role of Non-Coding RNAs in Stroke. *Stroke* **49**, 3098–3106 (2018).
1072 14. Leung, A. K. L. & Sharp, P. A. MicroRNA Functions in Stress Responses. *Mol Cell* **40**, 205–
1073 215 (2010).
1074 15. Denzler, R. *et al.* Impact of MicroRNA Levels, Target-Site Complementarity, and
1075 Cooperativity on Competing Endogenous RNA-Regulated Gene Expression. *Mol Cell* **64**, 565–
1076 579 (2016).

1077 16. Salmena, L., Poliseno, L., Tay, Y., Kats, L. & Pandolfi, P. P. A ceRNA hypothesis: the Rosetta
1078 Stone of a hidden RNA language? *Cell* **146**, 353–358 (2011).
1079 17. Franco-Zorrilla, J. M. *et al.* Target mimicry provides a new mechanism for regulation of
1080 microRNA activity. *Nat Genet* **39**, 1033–1037 (2007).
1081 18. Zhang, Y. *et al.* Circular RNAs in the Regulation of Oxidative Stress. *Frontiers in*
1082 *Pharmacology* **12**, (2021).
1083 19. Loo, L. *et al.* Single-cell transcriptomic analysis of mouse neocortical development. *Nat*
1084 *Commun* **10**, 134 (2019).
1085 20. Semenza, G. L. Hypoxia-inducible factor 1: control of oxygen homeostasis in health and
1086 disease. *Pediatr Res* **49**, 614–617 (2001).
1087 21. Zhang, J., Chen, S., Yang, J. & Zhao, F. Accurate quantification of circular RNAs identifies
1088 extensive circular isoform switching events. *Nat Commun* **11**, 90 (2020).
1089 22. Loppi, S. *et al.* Peripheral inflammation preceeding ischemia impairs neuronal survival through
1090 mechanisms involving miR-127 in aged animals. *Aging Cell* **20**, e13287 (2021).
1091 23. Step, S. E. *et al.* Anti-diabetic rosiglitazone remodels the adipocyte transcriptome by
1092 redistributing transcription to PPARγ-driven enhancers. *Genes Dev* **28**, 1018–1028 (2014).
1093 24. Meng, F.-L. *et al.* Convergent transcription at intragenic super-enhancers targets AID-initiated
1094 genomic instability. *Cell* **159**, 1538–1548 (2014).
1095 25. Min, I. M. *et al.* Regulating RNA polymerase pausing and transcription elongation in
1096 embryonic stem cells. *Genes & Development* **25**, 742 (2011).
1097 26. Fang, B. *et al.* Circadian enhancers coordinate multiple phases of rhythmic gene transcription in
1098 vivo. *Cell* **159**, 1140–1152 (2014).
1099 27. Hah, N. *et al.* Inflammation-sensitive super enhancers form domains of coordinately regulated
1100 enhancer RNAs. *Proceedings of the National Academy of Sciences* **112**, E297–E302 (2015).

1101 28. Heinz, S. *et al.* Effect of natural genetic variation on enhancer selection and function. *Nature*
1102 **503**, 487–492 (2013).
1103 29. Escoubet-Lozach, L. *et al.* Mechanisms Establishing TLR4-Responsive Activation States of
1104 Inflammatory Response Genes. *PLOS Genetics* **7**, e1002401 (2011).
1105 30. Ji, Z. *et al.* Transcriptional activity regulates alternative cleavage and polyadenylation. *Mol Syst*
1106 *Biol* **7**, 534 (2011).
1107 31. Zhang, F. *et al.* Enhancer-bound LDB1 regulates a corticotrope promoter-pausing repression
1108 program. *Proceedings of the National Academy of Sciences* **112**, 1380–1385 (2015).
1109 32. Telese, F. *et al.* LRP8-Reelin-regulated Neuronal (LRN) Enhancer Signature Underlying
1110 Learning and Memory Formation. *Neuron* **86**, 696–710 (2015).
1111 33. Sticht, C., Torre, C. D. L., Parveen, A. & Gretz, N. miRWalk: An online resource for prediction
1112 of microRNA binding sites. *PLOS ONE* **13**, e0206239 (2018).
1113 34. Dweep, H. & Gretz, N. miRWalk2.0: a comprehensive atlas of microRNA-target interactions.
1114 *Nat Methods* **12**, 697–697 (2015).
1115 35. Zeisel, A. *et al.* Molecular Architecture of the Mouse Nervous System. *Cell* **174**, 999-1014.e22
1116 (2018).
1117 36. Yoon, J. S. *et al.* Spatiotemporal Protein Atlas of Cell Death-Related Molecules in the Rat
1118 MCAO Stroke Model. *Exp Neurobiol* **27**, 287–298 (2018).
1119 37. Kabaria, S. *et al.* MicroRNA-7 activates Nrf2 pathway by targeting Keap1 expression. *Free*
1120 *Radic Biol Med* **89**, 548–556 (2015).
1121 38. Chaudhuri, A. D., Kabaria, S., Choi, D. C., Mouradian, M. M. & Junn, E. MicroRNA-7
1122 Promotes Glycolysis to Protect against 1-Methyl-4-phenylpyridinium-induced Cell Death. *J*
1123 *Biol Chem* **290**, 12425–12434 (2015).

1124 39. LaPierre, M. P., Lawler, K., Godbersen, S., Farooqi, I. S. & Stoffel, M. MicroRNA-7 regulates
1125 melanocortin circuits involved in mammalian energy homeostasis. *Nat Commun* **13**, 5733
1126 (2022).
1127 40. Tan, C. L. *et al.* MicroRNA-128 Governs Neuronal Excitability and Motor Behavior in Mice.
1128 *Science* **342**, 1254–1258 (2013).
1129 41. Chen, H. *et al.* miR-7 and miR-214 are specifically expressed during neuroblastoma
1130 differentiation, cortical development and embryonic stem cells differentiation, and control
1131 neurite outgrowth in vitro. *Biochemical and Biophysical Research Communications* **394**, 921–
1132 927 (2010).
1133 42. Rybak-Wolf, A. *et al.* Circular RNAs in the Mammalian Brain Are Highly Abundant,
1134 Conserved, and Dynamically Expressed. *Mol Cell* **58**, 870–885 (2015).
1135 43. Noh, K.-M. *et al.* Blockade of calcium-permeable AMPA receptors protects hippocampal
1136 neurons against global ischemia-induced death. *Proc Natl Acad Sci U S A* **102**, 12230–12235
1137 (2005).
1138 44. Yao, G.-Y. *et al.* Ischemic postconditioning confers cerebroprotection by stabilizing VDACs
1139 after brain ischemia. *Cell Death Dis* **9**, 1–15 (2018).
1140 45. Zhao, J. & Wang, B. MiR-7-5p Enhances Cerebral Ischemia-Reperfusion Injury by Degrading
1141 sirt1 mRNA. *J Cardiovasc Pharmacol* **76**, 227–236 (2020).
1142 46. Mehta, S. L. *et al.* CDR1as regulates α-synuclein-mediated ischemic brain damage by
1143 controlling miR-7 availability. *Mol Ther Nucleic Acids* **31**, 57–67 (2023).
1144 47. Bushati, N. & Cohen, S. M. microRNA functions. *Annu Rev Cell Dev Biol* **23**, 175–205 (2007).
1145 48. Miska, E. A. *et al.* Most Caenorhabditis elegans microRNAs are individually not essential for
1146 development or viability. *PLoS Genet* **3**, e215 (2007).
1147 49. Korvenlaita, N. *et al.* Dynamic release of neuronal extracellular vesicles containing miR-21a-5p
1148 is induced by hypoxia. *Journal of Extracellular Vesicles* **12**, 12297 (2023).

1149 50. Tiihonen, J. *et al.* Sex-specific transcriptional and proteomic signatures in schizophrenia. *Nat*
1150 *Commun* **10**, 3933 (2019).
1151 51. Kumar, M. & Katyal, A. Data on retinoic acid and reduced serum concentration induced
1152 differentiation of Neuro-2a neuroblastoma cells. *Data in Brief* **21**, 2435–2440 (2018).
1153 52. Korhonen, P. *et al.* Immunomodulation by interleukin-33 is protective in stroke through
1154 modulation of inflammation. *Brain, Behavior, and Immunity* **49**, 322–336 (2015).
1155 53. Majid, A. *et al.* Differences in vulnerability to permanent focal cerebral ischemia among 3
1156 common mouse strains. *Stroke* **31**, 2707–2714 (2000).
1157 54. Marques, S. M. *et al.* Genetic background determines mouse strain differences in inflammatory
1158 angiogenesis. *Microvasc Res* **82**, 246–252 (2011).
1159 55. Shahjouei, S. *et al.* Middle Cerebral Artery Occlusion Model of Stroke in Rodents: A Step-by-
1160 Step Approach. *J Vasc Interv Neurol* **8**, 1–8 (2016).
1161 56. Senda, D. M., Franzin, S., Mori, M. A., de Oliveira, R. M. W. & Milani, H. Acute, post-
1162 ischemic sensorimotor deficits correlate positively with infarct size but fail to predict its
1163 occurrence and magnitude after middle cerebral artery occlusion in rats. *Behav Brain Res* **216**,
1164 29–35 (2011).
1165 57. Schneider, C. A., Rasband, W. S. & Eliceiri, K. W. NIH Image to ImageJ: 25 years of image
1166 analysis. *Nat Methods* **9**, 671–675 (2012).
1167 58. Zhang, J., Chen, S., Yang, J. & Zhao, F. Accurate quantification of circular RNAs identifies
1168 extensive circular isoform switching events. *Nat Commun* **11**, 90 (2020).
1169 59. Law, C. W. *et al.* RNA-seq analysis is easy as 1-2-3 with limma, Glimma and edgeR. *F1000Res*
1170 **5**, (2016).
1171 60. Robinson, M. D. & Oshlack, A. A scaling normalization method for differential expression
1172 analysis of RNA-seq data. *Genome Biol* **11**, R25 (2010).

1173 61. Zhang, Z. *et al.* Novel Data Transformations for RNA-seq Differential Expression Analysis. *Sci*
1174 *Rep* **9**, 4820 (2019).
1175 62. Gu, Z., Schlesner, M. & Hübschmann, D. cola: an R/Bioconductor package for consensus
1176 partitioning through a general framework. *Nucleic Acids Research* **49**, e15 (2021).
1177 63. Zhang, Y., Parmigiani, G. & Johnson, W. E. ComBat-seq: batch effect adjustment for RNA-seq
1178 count data. *NAR Genomics and Bioinformatics* **2**, lqaa078 (2020).
1179 64. Allswede, D. M. *et al.* Complement Gene Expression Correlates with Superior Frontal Cortical
1180 Thickness in Humans. *Neuropsychopharmacol.* **43**, 525–533 (2018).
1181 65. Winsor, C. P., Hastings, C., Mosteller, F. & Tukey, J. W. Low Moments for Small Samples: A
1182 Comparative Study of Order Statistics. *The Annals of Mathematical Statistics* (1947)
1183 doi:10.1214/aoms/1177730388.
1184 66. Benjamini, Y. & Hochberg, Y. Controlling the False Discovery Rate: A Practical and Powerful
1185 Approach to Multiple Testing. *Journal of the Royal Statistical Society: Series B*
1186 *(Methodological)* **57**, 289–300 (1995).
1187 67. Krämer, A., Green, J., Pollard, J. & Tugendreich, S. Causal analysis approaches in Ingenuity
1188 Pathway Analysis. *Bioinformatics* **30**, 523–530 (2014).
1189 68. Zhou, Y. *et al.* Metascape provides a biologist-oriented resource for the analysis of systems-
1190 level datasets. *Nat Commun* **10**, 1523 (2019).
1191 69. Loo, L. *et al.* Single-cell transcriptomic analysis of mouse neocortical development. *Nat*
1192 *Commun* **10**, 134 (2019).
1193 70. Dong, M. *et al.* SCDC: bulk gene expression deconvolution by multiple single-cell RNA
1194 sequencing references. *Briefings in Bioinformatics* **22**, 416–427 (2021).
1195 71. Zeisel, A. *et al.* Molecular Architecture of the Mouse Nervous System. *Cell* **174**, 999-1014.e22
1196 (2018).

1197 72. Wang, X., Park, J., Susztak, K., Zhang, N. R. & Li, M. Bulk tissue cell type deconvolution with
1198 multi-subject single-cell expression reference. *Nat Commun* **10**, 380 (2019).
1199 73. Heinz, S. *et al.* Simple combinations of lineage-determining transcription factors prime cis-
1200 regulatory elements required for macrophage and B cell identities. *Mol Cell* **38**, 576–589
1201 (2010).
1202 74. Blankenberg, D. *et al.* Manipulation of FASTQ data with Galaxy. *Bioinformatics* **26**, 1783
1203 (2010).
1204 75. Langmead, B., Trapnell, C., Pop, M. & Salzberg, S. L. Ultrafast and memory-efficient
1205 alignment of short DNA sequences to the human genome. *Genome Biology* **10**, R25 (2009).
1206 76. Dweep, H. & Gretz, N. miRWalk2.0: a comprehensive atlas of microRNA-target interactions.
1207 *Nat Methods* **12**, 697–697 (2015).
1208 77. Sticht, C., Torre, C. D. L., Parveen, A. & Gretz, N. miRWalk: An online resource for prediction
1209 of microRNA binding sites. *PLOS ONE* **13**, e0206239 (2018).
1210 78. Smirnov, N. Table for Estimating the Goodness of Fit of Empirical Distributions. *The Annals of*
1211 *Mathematical Statistics* **19**, 279–281 (1948).
1212 79. Eichhorn, S. W. *et al.* mRNA destabilization is the dominant effect of mammalian microRNAs
1213 by the time substantial repression ensues. *Mol Cell* **56**, 104–115 (2014).
1214 80. Kantorovich, L. V. Mathematical Methods of Organizing and Planning Production.
1215 *Management Science* **6**, 366–422 (1960).
1216 81. Martin, M. Cutadapt removes adapter sequences from high-throughput sequencing reads.
1217 *EMBnet.journal* **17**, 10–12 (2011).
1218 82. Li, H. & Durbin, R. Fast and accurate short read alignment with Burrows–Wheeler transform.
1219 *Bioinformatics* **25**, 1754–1760 (2009).
1220 83. Trapnell, C., Pachter, L. & Salzberg, S. L. TopHat: discovering splice junctions with RNA-Seq.
1221 *Bioinformatics* **25**, 1105–1111 (2009).

1222 84. Kd, P., T, T. & Dr, M. NCBI Reference Sequence (RefSeq): a curated non-redundant sequence
1223 database of genomes, transcripts and proteins. *Nucleic acids research* **33**, (2005).
1224 85. Glažar, P., Papavasileiou, P. & Rajewsky, N. circBase: a database for circular RNAs. *RNA* **20**,
1225 1666–1670 (2014).
1226 86. Machanick, P. & Bailey, T. L. MEME-ChIP: motif analysis of large DNA datasets.
1227 *Bioinformatics* **27**, 1696–1697 (2011).
1228